

Elastic least-squares migration for quantitative reflection imaging of fracture compliances

Minato, Shohei; Wapenaar, Kees; Ghose, Ranajit

DOI

[10.1190/geo2019-0703.1](https://doi.org/10.1190/geo2019-0703.1)

Publication date

2020

Document Version

Accepted author manuscript

Published in

Geophysics

Citation (APA)

Minato, S., Wapenaar, K., & Ghose, R. (2020). Elastic least-squares migration for quantitative reflection imaging of fracture compliances. *Geophysics*, *85*(6), S327 - S342. <https://doi.org/10.1190/geo2019-0703.1>

Important note

To cite this publication, please use the final published version (if applicable).
Please check the document version above.

Copyright

Other than for strictly personal use, it is not permitted to download, forward or distribute the text or part of it, without the consent of the author(s) and/or copyright holder(s), unless the work is under an open content license such as Creative Commons.

Takedown policy

Please contact us and provide details if you believe this document breaches copyrights.
We will remove access to the work immediately and investigate your claim.

Elastic least-squares migration for quantitative reflection imaging of fracture compliances

Shohei Minato^{*†}, Kees Wapenaar^{*} and Ranajit Ghose^{*}

^{}Delft University of Technology, Department of Geoscience and Engineering, Delft,
2628CN, The Netherlands. Email: s.minato-1@tudelft.nl (corresponding author);*

c.p.a.wapenaar@tudelft.nl; r.ghose@tudelft.nl.

[†]OYO Corporation, Research and Development Center, Saitama, 331-0812, Japan.

(October 15, 2020)

Running head: **Imaging fracture compliances using LSM**

ABSTRACT

To quantitatively image fractures with high resolution, we develop an elastic least-squares migration (LSM) algorithm coupled with linear-slip theory, which accurately addresses seismic wave interaction with thin structures. We derive a linearized waveform inversion using the Born approximation to the boundary integral equation for scattered waves, including linear-slip interfaces for P-SV and SH wavefields. Numerical modeling tests assuming a laboratory-scale fracture where a 20 cm long fracture is illuminated by waves with 50 KHz center frequency, show that the proposed LSM successfully estimates the fracture compliances. Furthermore, due to the presence of coupling compliances at the fracture, the results using the proposed LSM show better images than those using the conventional LSM estimating Lamé constants. We also numerically illustrate that the proposed LSM can be successfully applied to dipole acoustic borehole logging data with 3 KHz center frequency

for single-well reflection imaging of a 10 m long, dipping fracture embedded in a random background. Finally, we apply the LSM to laboratory experimental data, measuring PP reflections from a fluid-filled fracture. We confirm that the estimated fracture compliances correspond well to those estimated by earlier AVO inversion. Furthermore, the LSM resolves the spatially varying fracture compliances due to local filling of water in the fracture. Because the linear-slip theory can be applied to thin structures in a wide range of scales, high-resolution imaging results and estimated fracture compliance distributions will be crucial to further address small-scale properties at fractures, joints and geological faults.

INTRODUCTION

Fractures and faults are mechanical weaknesses in the subsurface. They extend, propagate, and connect and interact with each other. Large-scale geological faults are generally associated with the accumulation of tectonic displacements (Ben-Zion and Sammis, 2003). Joints and geological faults in low-porosity rocks and deformation bands in highly porous rocks are fluid pathways or fluid barriers, and therefore control the subsurface mechanical and hydraulic properties (Aydin, 2000; Fossen et al., 2007). Due to the sensitivity of seismic waves to mechanical properties, seismic fracture characterization has provided vital information of fractures in the upper crust of the Earth (e.g., Leary et al., 1990; Liu and Martinez, 2013).

Fractures, joints and faults can be thought of as thin structures, with their thicknesses being significantly smaller than their length (e.g., Segall and Pollard, 1980). Seismic wave propagation across a compliant zone that is thin with respect to the seismic wavelength is often represented by the linear-slip theory (Schoenberg, 1980). The theory assumes a thin compliant zone to be a zero-thickness nonwelded interface: seismic wave traction is continuous across the interface but seismic wave displacement is discontinuous. The magnitude of the displacement discontinuity is controlled by the traction vector and the fracture compliance tensor.

The fracture compliance tensor represents the small-scale properties at the thin compliant zone. The linear-slip theory can accurately represent a wide variety of structures that are thin with respect to the seismic wavelength, e.g., a fracture having rough surfaces, a thin layer of a visco-elastic material or a poro-elastic material (Nagy, 1992; Worthington and Hudson, 2000; Barbosa et al., 2017). The nonwelded interface model has been tested for thin structures in a wide range of scales, e.g., cracks in metals, fractures and joints in

rocks, and geological faults (e.g., Rokhlin and Wang, 1991; Pyrak-Nolte and Nolte, 1992; Worthington and Hudson, 2000; Li et al., 2014a; Minato and Ghose, 2016a). Worthington (2007) and Hobday and Worthington (2012) discuss the possibility that fracture compliance increases with fracture size. Furthermore, anisotropy caused by fracture compliance tensor enables determining the preferred orientation of a rough surface due to slickenside and striations (Bakulin et al., 2000b; Far et al., 2013), and the off-diagonal components of a fracture compliance tensor are sensitive to the shear-induced altered distribution of the contacts (Nakagawa et al., 2000). Kame et al. (2014) discuss the relation between the linear-slip theory and the change of the strength of faults using stick-slip cycle experiments. Finally, the fracture compliances are relevant to the bulk deformation of a fracture under static loading (Hobday and Worthington, 2012, and references therein).

Earlier studies of seismic fracture characterization assume that the seismic wavelength is not capable of resolving the fine details of individual fractures and that a low frequency/long wavelength seismic wave only senses the cumulative effect of multiple fractures whose spacing is much smaller than the seismic wavelength. In this case, individual fractures are considered seismically invisible, but multiple fractures effectively change the elastic properties of the representative elementary volume into anisotropy (e.g., Crampin, 1984). The linear-slip theory is exploited to link the averaged fracture compliance tensor of multiple fractures to seismic anisotropy (e.g., Bakulin et al., 2000a).

Although the approach of seismic anisotropy based on an effective medium assuming small fractures has been successful to characterize a fractured medium (Leary et al., 1990; Liu and Martinez, 2013, among many others), large-scale fractures dominate hydraulic and mechanical properties of the entire subsurface (e.g., Aydin, 2000). Furthermore, as noted in Segall and Pollard (1980), discontinuous fault traces occur at all length scales. When the

fracture length and spacing are larger than or comparable to the seismic wavelength, the effective medium approach shows large errors due to neglected scattered waves (Yousef and Angus, 2016). In this vein, there is a growing number of reports showing scattered waves, including reflected waves, due to thin compliant zones like fractures, joints and geological faults. For example, reflection imaging methods using acoustic logging data have shown the potential to image fine-scale structures including fractures (Hornby, 1989; Tang and Patterson, 2009). The recent developments of dipole acoustic logging enabled imaging of fine structures up to 40 meters away from the borehole (Lee et al., 2019). Reshetnikov et al. (2010) use reflection events in microseismic data at the San Andreas Fault zone and imaged a thin fault layer intersecting the borehole and a fault inside the fractured sandstone. Despite these imaging results, the characterization of elastic properties of those thin compliant zones has not yet been possible due to the lack of high-resolution characterization methodologies.

Several methods that do not rely on the effective medium approach have been proposed for characterizing large-scale fractures using scattered waves. Willis et al. (2006) consider scattered waves due to multiple fractures and estimate fracture orientations, exploiting the azimuthal variation of a scattering index. Elastic compliances of an individual fracture have been estimated through AVO inversion of primary reflections (Minato and Ghose, 2016a; Peng et al., 2017; Minato et al., 2018) and using data-driven wavefield reconstruction of scattered waves (Minato and Ghose, 2014, 2016b). Cui et al. (2017) discuss the feasibility of the AVO inversion with fracture compliances in the seismic frequency range. Pourahmadian et al. (2017) also develop an inversion approach to estimate the spatially varying fracture compliance using a generalized linear sampling method. Characterization of fractures intersecting a borehole was also performed using transmitted waves in acoustic logging data (Barbosa et al., 2019) and tube wave scattering in vertical seismic profiling

data (Hardin et al., 1987; Minato et al., 2017).

The existing approaches discussed above involve a two-step processing to estimate the fracture compliances: imaging the fracture geometry followed by estimating the fracture compliances at the known fracture geometry. In this study, we develop an alternative approach which handles multiple fractures with unknown geometry embedded in a complex background medium. To this end, we explore least-squares migration (LSM) of reflection data, with fractures represented by the linear-slip theory.

Seismic migration methods, aimed at high-resolution imaging in complex media, are formulated as a linearized waveform inversion to estimate quantitative medium properties. Those properties are reflectivity (e.g., angle-dependent reflection coefficients) based on the Kirchhoff approximation (Xu et al., 2001, 2011) or perturbation of medium properties in the volume (e.g., Lamé constants and density) based on the Born approximation (Tarantola, 1984). These migration/inversion methods can be implemented as ray-based asymptotic inversion (Bleistein, 1987), or as a general least-squares problem (Tarantola, 1984). The latter approach can be implemented by numerically solving a linear discrete inverse problem, which is what we call LSM in this study. The LSM is known to be robust to acquisition irregularities and incomplete data (Nemeth et al., 1999).

In the framework of migration/inversion mentioned above, quantitative medium properties are estimated differently. The algorithms based on the Born approximation directly estimate the spatial distribution of medium properties defined in the volume, e.g., perturbations in velocity/slowness (Lambaré et al., 1992; Plessix and Mulder, 2004), or those in Lamé constants, density and impedance (Beydoun and Mendes, 1989; Jin et al., 1992; Operto et al., 2000). On the other hand, angle-dependent reflection coefficients estimated

by methods based on the Kirchhoff approximation (Xu et al., 2001, 2011) are properties defined at an interface between two different media. Therefore, to further elucidate the medium properties in the volume, amplitude variation with offset/angle (AVO/AVA) inversion is applied to the estimated reflection coefficients (Tura et al., 1998). All conventional migration approaches mentioned above assume perfectly welded interfaces without fracture compliances; the nonwelded interface with the fracture compliance tensor has not been considered in migration/inversion.

In this study, we develop a new LSM for quantitatively imaging thin compliance zones like fractures using the linear-slip model. The linearized equation is derived from the Born approximation using the elastic wave representation theorem including nonwelded boundary conditions (Wapenaar, 2007). This, in combination with a singular function (Bleistein, 1987; Bostock, 2002), enables us to directly estimate the spatial distribution of the fracture compliance tensor which is defined at an interface. Note that an approach using the Kirchhoff approximation, instead of the Born approximation, is also possible. In this case, we estimate angle- and frequency-dependent reflection coefficients due to the fracture compliances, which will provide input data for AVO/AVA inversion of fractures (Minato and Ghose, 2016a; Cui et al., 2017; Peng et al., 2017; Minato et al., 2018). In this study, however, we restrict ourselves to the Born approximation so that we directly estimate the spatial distribution of fracture compliances without the two-step processing mentioned earlier.

This paper is organized as follows. We first explain the boundary conditions of the nonwelded interface model. Next, we introduce the definition of the 2D problem considered in this study, i.e., wave propagation in a 2D ($x - z$) plane in an isotropic medium where the vector normal to a fracture surface is located in the same plane, and the values of the fracture compliance tensors associated to the y axis are negligible. In this case, we

separately consider P-SV and SH wavefields. We then formulate the new LSM as a linearized waveform inversion to estimate the fracture compliances using the Born approximation. We discuss numerical modeling examples representing a horizontal fracture in laboratory-scale measurements, to show the quantitative nature of LSM, and the relation between the new LSM and conventional LSM associated to a thin-layer model of fractures. We also perform numerical experiments representing borehole acoustic logging measurements to characterize a dipping fracture embedded in a random background medium. Finally, we show the results of the application of the new LSM to data from ultrasonic laboratory experiments with a fluid-filled fracture.

THEORY

Nonwelded interface model for thin structures

We consider that the seismic wavelength is much larger than the aperture of a fracture and the characteristic wavelength of the contact asperity distribution at the rough surface of the fracture. In this case, the fracture can be represented by a compliant and nonwelded interface, where a fracture-compliance tensor describes the magnitude of deformation at the interface. The linear-slip theory (Schoenberg, 1980) considers that the deformation at the interface (seismic-induced displacement jump) linearly depends on the seismic traction and the fracture compliance tensor:

$$\begin{pmatrix} \Delta u_x \\ \Delta u_y \\ \Delta u_z \end{pmatrix} = \boldsymbol{\eta} \begin{pmatrix} \tau_{xz} \\ \tau_{yz} \\ \tau_{zz} \end{pmatrix}, \quad (1)$$

where $\boldsymbol{\eta}$ is the fracture compliance tensor:

$$\boldsymbol{\eta} = \begin{pmatrix} \eta_{xx} & \eta_{xy} & \eta_{xz} \\ \eta_{yx} & \eta_{yy} & \eta_{yz} \\ \eta_{zx} & \eta_{zy} & \eta_{zz} \end{pmatrix}. \quad (2)$$

We assume here that the fracture surface is located in the $x - y$ plane. In equation 1, Δu_i is the discontinuity in the displacement in the i direction across the fracture, and τ_{ij} is the stress field, where the subscripts i and j can each stand for x , y or z . The linear-slip theory assumes the stress across the fracture to be continuous. In equation 2, each element of the fracture compliance tensor describes the magnitude of the displacement discontinuity due to different traction component. The simplest form of the fracture compliance tensor is a diagonal matrix assuming rotational symmetry (Schoenberg, 1980). In this case, the fracture compliance tensor is written as,

$$\boldsymbol{\eta} = \text{diag}(\eta_T, \eta_T, \eta_N), \quad (3)$$

where *diag* indicates a diagonal matrix. In equation 3, η_T is the tangential compliance and η_N the normal compliance, respectively due to tangential stress and normal stress. Several theoretical models have been developed in the past to relate the fracture compliances to small-scale heterogeneities at a fracture, e.g., a thin layer of visco-elastic material (Schoenberg, 1980; Rokhlin and Wang, 1991), a thin layer of poro-elastic material (Nakagawa and Schoenberg, 2007; Barbosa et al., 2017), or statistical properties of contact asperities (Worthington and Hudson, 2000). Importantly, any compliant structure whose thickness is thin compared to the seismic wavelength is appropriately represented by the nonwelded interface model, e.g., fractures, joints and faults.

Uncoupled P-SV and SH wavefields

In this study, we consider 2D wave propagation in the $x - z$ plane, assuming that variations in elastic constants and density along the y axis are negligible. Furthermore, a point source in the $x - z$ plane in the numerical modeling examples discussed in the later sections corresponds to a line source along the y axis. In this case, P-SV wave components ($v_x, v_z, \tau_{xx}, \tau_{zz}, \tau_{xz}$) and SH wave components ($v_y, \tau_{xy}, \tau_{yz}$) are mutually uncoupled when they are independent of each other in the constitutive equations (e.g., in the case of isotropic background medium), and in the linear-slip boundary condition (equation 1). The latter is the case when the fracture compliance tensor (equation 2) has the following form:

$$\boldsymbol{\eta}_h = \begin{pmatrix} \eta_{T_1} & 0 & \eta_C \\ 0 & \eta_{T_2} & 0 \\ \eta_C & 0 & \eta_N \end{pmatrix}, \quad (4)$$

where η_C is the coupling compliance. The tangential fracture compliances in two principle directions (η_{T_1} and η_{T_2}) may have different values (Bakulin et al., 2000b; Far et al., 2013); subscript h indicates a horizontal fracture. The coupling compliance η_C in equation 4 indicates the tangential deformation (Δu_x) due to normal stress (τ_{zz}) or the normal deformation (Δu_z) due to tangential stress (τ_{xz}); the existence of the coupling compliance has earlier been shown in laboratory experiments and by numerical calculation considering a periodic crack model (Nakagawa et al., 2000). The zero off-diagonal components in equation 4 assume that variations in the small-scale structures (e.g., periodic shape) at the fracture along the y axis are negligible.

Next, we show that P-SV and SH wavefields are uncoupled for a dipping fracture in the $x - z$ plane. We first consider the general nonwelded-interface boundary condition

(Wapenaar, 2007):

$$[\mathbf{M}\mathbf{u}] = -j\omega\mathbf{Y}\langle\mathbf{M}\mathbf{u}\rangle, \quad (5)$$

where $j = \sqrt{-1}$, ω is the angular frequency, \mathbf{u} the complete wave vector, \mathbf{M} a matrix contracting \mathbf{u} to the components involved in the boundary condition (e.g., traction vector), \mathbf{Y} a matrix including the boundary parameters (e.g., a fracture compliance tensor), and $[\cdot]$ and $\langle\cdot\rangle$ represent the jump and average across the interface, respectively. The explicit forms of the vectors and matrices in equation 5 depend on the dimensionality of the problem and the wave modes. In a 3D elastodynamic wavefield, \mathbf{u} is a 12×1 vector including particle velocities and stresses, \mathbf{M} a 6×12 matrix and \mathbf{Y} a 6×6 matrix (Wapenaar et al., 2004).

In this case, equation 5 can be written as,

$$\begin{pmatrix} [\mathbf{v}] \\ -[\boldsymbol{\sigma}\mathbf{n}] \end{pmatrix} = -j\omega\mathbf{Y} \begin{pmatrix} \langle\mathbf{v}\rangle \\ -\langle\boldsymbol{\sigma}\mathbf{n}\rangle \end{pmatrix}, \quad (6)$$

where \mathbf{v} is the particle velocity vector, $\boldsymbol{\sigma}$ the Cauchy stress tensor, and $\mathbf{n} = (n_x, n_y, n_z)$ a fracture-normal vector. The linear-slip boundary condition for a horizontal fracture is derived from equation 6 by assuming $\mathbf{n} = (0, 0, 1)$ and the matrix \mathbf{Y} as,

$$\mathbf{Y}_h = \begin{pmatrix} \mathbf{0} & \boldsymbol{\eta}_h \\ \mathbf{0} & \mathbf{0} \end{pmatrix}. \quad (7)$$

Considering that a dipping fracture in the fracture-oriented coordinate system satisfies the same boundary condition as a horizontal fracture in the original coordinate system, we obtain the matrix \mathbf{Y} as a function of $\boldsymbol{\eta}_h$ for a dipping fracture with an arbitrary normal vector \mathbf{n} :

$$\mathbf{Y} = \begin{pmatrix} \mathbf{0} & \mathbf{Q}^T\boldsymbol{\eta}_h\mathbf{Q} \\ \mathbf{0} & \mathbf{0} \end{pmatrix}, \quad (8)$$

where \mathbf{Q} is the rotation matrix. Therefore, when a fracture is dipping in the $x-z$ plane, i.e., $\mathbf{n} = (n_x, 0, n_z)$ and $\mathbf{Q} = \begin{pmatrix} n_z & 0 & -n_x \\ 0 & 1 & 0 \\ n_x & 0 & n_z \end{pmatrix}$, then P-SV and SH wave components are uncoupled in the boundary condition (equation 6).

Elastic least-squares migration

For the quantitative reflection imaging that we propose in this study, we consider a linearized waveform inversion using the following equation:

$$\mathbf{d} = \mathbf{L}\mathbf{m}, \quad (9)$$

where \mathbf{d} is waveform data, \mathbf{m} the spatial distribution of material properties (e.g., reflectivity or perturbation in elastic constants) that produces scattered waves due to a source wavefield, and \mathbf{L} a Born or Kirchhoff operator. In the case of space-frequency domain, \mathbf{d} is a column vector with $N_f \times N_{tr}$ components, \mathbf{m} is a column vector with $M \times N_p$ components, and \mathbf{L} is a $N_f N_{tr} \times M N_p$ matrix, where N_{tr} is the total number of traces, N_f the total number of frequencies, M the total number of grid points in the imaging volume, and N_p the number of inversion parameters. Least-squares migration (LSM) solves equation 9 for \mathbf{m} , considering \mathbf{m} to be perturbations of material properties or reflectivity (Yang and Zhang, 2019, and references therein). Equation 9 can be derived after linearizing the full wavefield equation using the Born or Kirchhoff approximation. The operator \mathbf{L} contains the source wavefield and Green's functions between points of scattering and receiver locations. In the next subsection, we specify equation 9 using the linear-slip theory and the Born approximation applied to the scattered wavefield.

In this study, we formulate equation 9 in the space-frequency domain, and we solve equation 9 for the model parameter vector \mathbf{m} using the conjugate gradient least-squares

method (CGLS). Thus, we define the imaging result of the proposed LSM as,

$$\mathbf{m}_{LSM} = \mathbf{L}^{-g} \mathbf{d}^o, \quad (10)$$

where \mathbf{d}^o is the observed data vector and \mathbf{L}^{-g} is the generalized inverse (e.g., Menke, 1989) of the Born operator \mathbf{L} , which is implicitly calculated by the CGLS method. We solve the system of equation 9 after constructing \mathbf{L} . When the data and the imaging volume are large, constructing the full matrix \mathbf{L} and estimating \mathbf{L}^{-g} are prohibitively expensive. In this case, an alternative approach can be used to numerically implement \mathbf{L} and its mathematical adjoint operator using ray approximation (e.g., Lambaré et al., 1992), one-way wave equation (e.g., Kühn and Sacchi, 2003), two-way wave equation (e.g., Feng and Schuster, 2017; Chen and Sacchi, 2017), or multisource migration technology (Tang and Biondi, 2009; Dai et al., 2011; Huang and Schuster, 2012).

Note that the CGLS method iteratively updates the model parameter vector \mathbf{m} from the initial value ($\mathbf{m}_0 = \mathbf{0}$) to minimize the objective function $E(\mathbf{m}) = \frac{1}{2} \|\mathbf{d}^o - \mathbf{L}\mathbf{m}\|^2$. In this case, the gradient of the objective function with respect to the model parameter evaluated at the initial value can be written as (e.g., Plessix and Mulder, 2004),

$$\frac{\partial E(\mathbf{m}_0)}{\partial \mathbf{m}} = -\Re(\mathbf{L}^\dagger \mathbf{d}^o), \quad (11)$$

where \mathbf{L}^\dagger is the Hermitian transpose of \mathbf{L} . The real part of $\mathbf{L}^\dagger \mathbf{d}^o$ (denoted by \Re) corresponds to the zero-lag crosscorrelation between the source and receiver wavefields; equation 11 is equivalent to the classical crosscorrelation imaging condition (Claerbout, 1971). Note that an evaluation of equation 11 does not involve inverting the Born operator.

Born approximation to scattered waves due to linear-slip interfaces

Appropriately deriving the Born operator \mathbf{L} associated with the linearized model parameter vector \mathbf{m} is necessary for LSM. The earlier studies of LSM consider imaging the perturbations in elastic constants (Lamé constants λ and μ) and density (ρ) or the impedance contrasts (Beydoun and Mendes, 1989; Jin et al., 1992). For this purpose, the Born operator is derived from an integral representation of the scattered wavefield due to the perturbations in λ , μ and ρ (Wu and Aki, 1985). Contrary to these earlier studies, in this study, we derive the Born operator \mathbf{L} considering the fracture compliance tensor. This new formulation is derived from the elastic wavefield representation theorem including nonwelded interfaces (Wapenaar, 2007).

From a convolution-type representation for Green's functions including nonwelded interfaces (Wapenaar, 2007), we obtain the following boundary integral representation of scattered seismic waves in the space-frequency domain:

$$\mathbf{u}(\mathbf{x}') - \bar{\mathbf{u}}(\mathbf{x}') = - \int_{\partial D_{\text{int}}} \bar{\mathbf{G}}(\mathbf{x}', \mathbf{x}) \Delta \mathbf{H}^b(\mathbf{x}) \mathbf{u}(\mathbf{x}) d^2 \mathbf{x}, \quad (12)$$

where \mathbf{u} denotes the wave vector, \mathbf{G} the Green's matrix, and $\Delta \mathbf{H}^b$ the fracture contrast function (Wapenaar, 2007). The variables with a bar ($\bar{\cdot}$) indicate wavefields that are defined in an arbitrary reference medium. ∂D_{int} is the geometry of the nonwelded interface (fracture). In the forward problem, the surface integral is evaluated at a known fracture geometry. We assume in equation 12 that the reference medium has the same elastic constants distribution as the true medium; hence, the only difference between the reference medium and the true medium is the fracture. The explicit forms of the vectors and matrices in equation 12 depend on the dimensionality of the problem and on the wave modes. In this study, we consider a 2D problem, and we show the explicit forms of \mathbf{u} , \mathbf{G} and $\Delta \mathbf{H}^b$ for the

P-SV wavefield and the SH wavefield, respectively, in Appendix A.

The Born approximation is defined as the first-order term of the Neumann series expansion of equation 12 for \mathbf{u} :

$$\mathbf{u}^S(\mathbf{x}') = - \int_{\partial D_{\text{int}}} \bar{\mathbf{G}}(\mathbf{x}', \mathbf{x}) \Delta \mathbf{H}^b(\mathbf{x}) \bar{\mathbf{u}}(\mathbf{x}) d\mathbf{x}, \quad (13)$$

where the left-hand side of the equation is the scattered wave, i.e., the difference of the wave vector between the true and the reference media. Note that we have changed the surface integral ($\int_{\partial D_{\text{int}}} d^2\mathbf{x}$) to the contour integral ($\int_{\partial D_{\text{int}}} d\mathbf{x}$) because of the considered 2D problem. When we define the reference medium such that it does not contain fractures, the contrast function $\Delta \mathbf{H}^b$ is linear with respect to the fracture compliances (η_T , η_N , and η_C) at the fracture (see Appendix A).

We use equation 13 to formulate the linearized model (equation 9) so that \mathbf{d} contains the recorded reflected waves (particle velocities), \mathbf{m} the spatial distribution of the fracture compliances, and \mathbf{L} the operator including Green's functions in the reference medium, the source wavefield, and the fracture dip angle (see Appendix A). To this end, we introduce a singular function (Bleistein, 1987; Bostock, 2002) at the fracture geometry (∂D_{int}) in order to recast the contour integral in equation 13 as a 2D volume integral:

$$\mathbf{u}^S(\mathbf{x}') = - \int_V \bar{\mathbf{G}}(\mathbf{x}', \mathbf{x}) \delta_{\Sigma}(\mathbf{x}) \Delta \mathbf{H}^b(\mathbf{x}) \bar{\mathbf{u}}(\mathbf{x}) d^2\mathbf{x}, \quad (14)$$

where V is a 2D volume and $\delta_{\Sigma}(\mathbf{x})$ is the singular function with support on the fracture geometry. The definition of the singular function can be found in Appendix B. Due to the band limitation of the input reflection data, furthermore, LSM estimates a bandlimited representation of $\delta_{\Sigma}(\mathbf{x})$ scaled by the fracture compliances. In this study, we compensate for the scaling effect due to band limitation of the singular function by analyzing the output image of LSM (see Appendix B for more details). Note that, for the 3D problem, the 2D

volume integral in equation 14 becomes a 3D volume integral with a singular function with support on the fracture surface.

NUMERICAL MODELING EXAMPLES OF LEAST-SQUARES MIGRATION OF FRACTURE COMPLIANCES

In this section, we show numerical modeling examples at two different scales where fractures are imaged and characterized using the proposed LSM. The first example considers simple, laboratory-scale measurements where a single horizontal fracture is embedded in a homogeneous medium. We assume that the nonwelded interface model best describes the elastic reflections from a fracture, and we estimate the fracture compliances using the proposed LSM. We also test the conventional LSM formulated as perturbations in Lamé constants (Beydoun and Mendes, 1989; Jin et al., 1992), which implies that we interpret the observed data by a thin-layer model of fractures (e.g., Wu et al., 2005). We discuss the relation between the estimated images using both formulations (linear-slip and thin-layer models), and explain the advantages of the proposed LSM over the conventional approach. The second example shows the potential of applying the proposed LSM to field-scale measurements where dipole acoustic borehole logging data are used to image a dipping fracture around a borehole embedded in a random background medium.

Laboratory-scale fracture imaging: numerical tests

Model and data

We first present a numerical modeling example considering an ultrasonic laboratory experiment to characterize a single horizontal fracture (Figure 1a). A horizontal receiver array

measures the reflected waves due to sources located at the same level as the receiver array (e.g., Palmer et al., 1981). Note that this configuration is equivalent to a vertical receiver array recording reflected waves from a vertical fracture (e.g., Cheng and Sansalone, 1995). We consider a 2D problem and a fracture with coupling compliance. The fracture compliances are, respectively, $\eta_{T_1} = \eta_{T_2} = \eta_T = 4.5 \times 10^{-14}$ m/Pa, $\eta_N = 1.75 \times 10^{-14}$ m/Pa, and $\eta_C = 1.40 \times 10^{-14}$ m/Pa, and they are tapered at the edges (Figure 1b). The values of η_T and η_N are taken from laboratory experiments of the fracture compliances in a fluid-filled sandstone (Lubbe et al., 2008). The coupling compliance (η_C) is calculated assuming its relative magnitude (equation 5 in Nakagawa et al., 2000) to be 0.5. The elastic properties and density of the background material are $V_P = 6350$ m/s, $V_S = 3410$ m/s, and $\rho = 2500$ kg/m³, respectively.

We install two point sources located at the center and at the edge of the receiver array (Figure 1a), considering uneven illumination of the fracture from the sources. The observed wavefield at the receiver array is calculated in the frequency-wavenumber domain (wdSDD, Nakagawa et al., 2004), where we use a point-force source 2D Green's function representing incident waves. The source wavelet is a Ricker wavelet with 50 KHz center frequency. The example of the modeled shot gather (source $x = 0.15$ m) is shown for SH wavefield (Figure 1c) and P-SV wavefield (Figure 1d). We consider a horizontal force source (f_y) for the SH wavefield and a vertical force source (f_z) for the P-SV wavefield, respectively. Furthermore, we add random noise to the modeled responses; the signal-to-noise ratio (SNR) is 15 dB, where we define SNR as the ratio of the peak amplitude and the standard deviation of noise. Furthermore, to identify reflection and scattering modes, we calculate the travel times of the specular reflections (Figure 1e) and those of the non-specular reflections, assuming scattering at the fracture edges (Figure 1f).

The SH wavefield (Figure 1c) contains specular reflections (SS) and non-specular scattered waves (SSd) due to spatially varying compliances at the fracture edges (Minato et al., 2018). The P-SV wavefield (Figure 1d) shows converted waves (PS, SP, PSd, SPd) as well as pure modes (PP, SS, PPd, SSd). The amplitudes of PS and SP waves show an asymmetric variation along the receiver position (around 0.10 ms in v_x in Figure 1d). At the zero-offset trace (receiver $x = 0.15$ m), the event at 0.10 ms is a PS wave because of the absence of normally propagating shear waves from the source due to the radiation pattern; we observe non-zero PS reflection amplitude at normal incidence. The non-zero PS reflection coefficient at normal incidence is due to the presence of the coupling fracture compliance, where the tangential displacement discontinuity is generated by the normal stress acting on the rough fracture (Nakagawa et al., 2000).

In Appendix C, we show that the Born approximation accurately predicts the wavefield in this configuration, i.e., the magnitude of the fracture compliances and the center frequency. At high frequencies, however, the discrepancy between the Born approximation and the true response is large. See Appendix C for more details.

Imaging results

We apply the new LSM (equation 10) to SH wavefield (Figure 2). The grid spacing in the imaging area is 2 mm. We calculate free-space Green's functions in the 2D elastic homogeneous reference medium (de Hoop, 1995) to construct the Born operator. Figure 2a presents the initial gradient of the objective function without inversion or the result of the classical crosscorrelation imaging condition (equation 11). The amplitude of the initial gradient is normalized by the maximum value. Figure 2b is the result of the new LSM solved

by CGLS method after 100 iterations (the convergence of the residual is shown in Figure 2d). Note that the scaling effect due to the band-limited singular function is compensated for in the LSM image (Figure 2b) by analyzing the bandwidth of the output image at a representative location in the imaged fracture (see Appendix B for more details).

The final LSM result (Figure 2b) images the fracture with higher resolution than the initial gradient without inversion (Figure 2a) because after the iteration LSM removes the effect of the source wavelet and compensates the illumination pattern due to uneven distribution of sources (two sources are installed, see Figure 1a). Furthermore, the final LSM image provides the quantitative property of the fracture (fracture compliance). The location of the peak amplitudes in Figure 2b successfully estimates the fracture geometry, and the peak amplitudes at the fracture between $x = 0.10$ m and $x = 0.20$ m show an average value of 4.43×10^{-14} m/Pa with a standard deviation of 0.57×10^{-14} m/Pa. Therefore, LSM successfully estimates the tangential compliance (4.5×10^{-14} m/Pa, see Figure 1b). The final data residual of LSM (black solid line in Figure 2d) shows the effect of noise and the errors in the Born approximation.

To illustrate a relation between linear-slip and thin-layer models for fracture imaging, the conventional LSM formulated as perturbations in Lamé constants as model parameters (Beydoun and Mendes, 1989; Jin et al., 1992) is applied to the same dataset (Figure 2c) where we estimate the volumetric distribution of perturbation in shear modulus ($\Delta\mu$). Note that for a consistent comparison with the new LSM, we use the same theoretical Green's functions as for the proposed LSM in constructing the Born operator of the conventional LSM, instead of using the ray-approximated Green's functions as proposed in Beydoun and Mendes (1989). Conventional LSM has a resolution similar to the new LSM. This corresponds to the fact that the linear-slip interface model can represent a thin layer of isotropic

material at normal incidence in the long wavelength assumption (e.g., Rokhlin and Wang, 1991; Nagy, 1992), i.e., $\eta_T = H/\mu_0$ where H is the layer thickness and μ_0 is the shear modulus of the thin layer. This indicates that we can estimate tangential fracture compliance using the conventional LSM when we appropriately interpret the effective thickness of the imaged fracture. Furthermore, the small difference in the final residual between the proposed and conventional LSM approaches (Figure 2d) indicates that the linear-slip model and the thin-layer model can explain almost equally well the reflections from the fractures (Wu et al., 2005).

The new LSM applied to the P-SV wavefield estimates the fracture compliance tensor: tangential (η_T), normal (η_N), and coupling (η_C) compliances (Figure 3a–3c, respectively). Due to the complex wavefield including mode conversion and limited source illumination, the imaged fracture compliances show more noise and artefacts than the result using SH wavefield. Nevertheless, the new LSM provides the fracture geometry much better than the conventional LSM (Figures 3d and 3e) where the volumetric distribution of $\Delta\mu$ and $\Delta\lambda$ is estimated. Contrary to the result for the SH wavefield, here the large difference in the final residual between the proposed and the conventional LSM (Figure 3f) indicates that the fracture is not represented by a thin isotropic layer. This is because the normal-incident P wave produces converted S wave (see Figure 1d and the discussion in the previous subsection). A possible approach to improve the resolution of the conventional LSM is to introduce effective anisotropy (Coates and Schoenberg, 1995) in a thin-layer model, which provides more degrees of freedom in fitting the observed data.

We show that the proposed LSM is successfully applied to numerically modeled data with noise. The comparison between the proposed and conventional LSM results shows that the conventional LSM assuming isotropic media fails to image the fracture when the frac-

ture contains non-zero coupling compliances, which indicates that the new LSM is crucial for monitoring shear-induced coupling changes at fractures. The results using SH wavefield show that the conventional LSM also can be used to estimate tangential fracture compliances. Note, however, that when fracture compliances are of primary interest (see Introduction), the proposed LSM is useful because it directly estimates the fracture compliances and it does not require estimating the effective fracture thickness using the conventional LSM.

Borehole acoustic logging: numerical tests

Model and data

The second numerical example shows field-scale fracture imaging. We consider borehole acoustic logging experiments in order to image and characterize fractures around a borehole. Single-well reflection imaging using acoustic logging data carefully removes direct and borehole-coupled waves to isolate reflected waves (Li et al., 2014b, 2017, and references therein). In the context of single-well reflection imaging, several imaging approaches have been tested, e.g., Kirchhoff depth migration, prestack f-k migration, beamforming migration, and reverse-time migration (Hornby et al., 1989; Tang and Patterson, 2009; Li and Yue, 2015; Gong et al., 2018). We propose in this subsection the use of the new LSM for high-resolution quantitative imaging of the fractures around a borehole.

We consider a 2D plane which is formed by the borehole axis and the normal vector of a fracture ($x - z$ plane in Figure 4a). The dip angle of the fracture is 50° with respect to the x axis, and the fracture intersects the borehole. The geometry can be interpreted also as a dipping borehole penetrating a subvertical fracture (Tang and Patterson, 2009).

Considering prior successful imaging of fine-scale fractures using dipole acoustic logging (Lee et al., 2019), we model dipole data, i.e., horizontal force and horizontal component receiver. We separately consider P-SV and SH wavefields assuming a 2D configuration. In this study, furthermore, we ignore the presence of the borehole and model a point force source and the particle displacement in an elastic medium where the borehole source and the receiver would be located.

We consider a 20 m deep and 10 m wide imaging area (Figure 4a). We assume a random background medium where a random velocity distribution is superposed on the constant P-wave velocity (4000 m/s). The V_P/V_S is fixed at 1.74, and we assume a constant density of 2500 kg/m³. The autocorrelation function of the random distribution follows a von Kármán function with Hurst number 1, correlation length 0.1 m, and a variance of 10 % with respect to the background medium. The random background model is inspired by the work of Tang et al. (2016), who investigate the elastic scattering in borehole acoustic logging. The rotationally invariant fracture (i.e., no coupling compliance) has the following parameters: $\eta_T=1\times 10^{-11}$ m/Pa and $\eta_N=1\times 10^{-12}$ m/Pa. These compliances correspond to a fluid-filled fracture where the normal fracture compliance η_N is one order of magnitude smaller than the tangential compliance η_T (Lubbe et al., 2008). The order of magnitude of the tangential fracture compliance corresponds to the scale length of the fracture - to be a few tens of meters, assuming a trend of increasing fracture compliance with fracture size (Hobday and Worthington, 2012).

The P-SV and SH wavefields are separately modeled using a rotated staggered-grid finite-difference time-domain (FDTD) method (Saenger and Shapiro, 2002) where linear-slip interfaces are implemented through calculating effective elastic properties (Coates and Schoenberg, 1995). We consider a realistic source and receiver configuration for dipole

acoustic measurements; the receiver array consists of five receivers with minimum offset 3 m and receiver spacing 0.15 m, and the tool moves along the borehole in steps of 0.5 m (e.g., Li et al., 2017). See Figure 4a for the source–receiver configuration. The dominant frequency of the dipole measurements is considered in the source wavelet; a Ricker wavelet with 3 KHz center frequency is used.

Figures 4b and 4c show, respectively, the examples of the modeled SH and P-SV wavefields, for the first receiver in the receiver array with varying source depths (i.e., a common receiver gather). Direct P and S waves have been suppressed in Figures 4b and 4c by subtracting the response of the reference medium from the modeled response. The reference medium is a homogeneous medium without the fracture with the background P- and S-wave velocities ($V_P = 4000$ m/s and $V_S = 2300$ m/s). Note that the reference medium is also utilized in calculating the Green’s functions in the proposed LSM. Figures 4d shows the traveltimes of direct waves (P and S) and reflected waves (PP, SS, PS and SP) calculated by using the reference medium and the fracture geometry. Although we ignore the borehole-coupled waves (Stoneley and flexural waves), the traveltimes of these waves are also calculated from the low-frequency approximation (White, 1983). Note that the flexural wave velocity is close to the formation shear-wave velocity at low frequencies in the fast formations, where V_S is larger than the compressional velocity of the borehole fluid (Tang and Patterson, 2010). At sources shallower than 5 m and those deeper than 12 m, the reflected waves, especially the SS waves, can be observed without major interferences with the direct waves (Figures 4d). However, suppressing the direct waves helps imaging the fracture close to the borehole between 5 m and 12 m depth. Direct waves are not perfectly suppressed in the data (see 2 ms and 0–6 m depth in Figures 4b and 4c) because of the random background velocity. The vertical event at 2 ms between 6–12 m depth in Figures 4b

and 4c is the transmitted wave across the fracture, and the dipping events are the reflected waves. As expected from dipole measurements, pure shear waves are dominant in the P-SV wavefield (SS), but converted waves (PS and SP waves) also show large amplitudes in the data where sources are located close to the fracture.

Imaging results

The proposed LSM (equation 10) is applied to the SH wavefield (Figure 5). The imaging area is discretized with a spatial sampling interval of 0.05 m; we use frequencies in the range of 0–8 KHz. We assume the source wavelet to be known: calibration of source wavelets can be performed using, for example, reference data with known reflection coefficients (see next section). Furthermore, we assume the fracture dip angle to be known in constructing the Born operator \mathbf{L} of both SH and P-SV wavefields: the information can be obtained from borehole acoustic/optical televiewer and/or conventional migration images. Note that the fracture dip angles can be assigned at each imaging grid point.

The strong artefacts in the initial gradient without inversion or the image with cross-correlation imaging condition (equation 11) around the borehole (around $x = 0$ m in Figure 5a) are due to the correlation of the remaining direct and transmitted waves with the source wavefield. The artefacts are largely suppressed in the final LSM image. The initial gradient does not provide quantitative information. In contrast, the new LSM minimizes the data misfit taking into account scattered radiation pattern at a fracture. This quantitative nature of LSM suppresses structures producing non-physical reflections. The effective wavelength in the LSM image is smaller than in the initial gradient (see insets figures in Figure 5a and 5b), which provides a much higher resolution image. Furthermore, the final

LSM image shows quantitative values of the fracture compliance (η_T). The peak amplitudes of the imaged η_T at the fracture between $x = -4$ m and $x = -1$ m show an average value of 6.47×10^{-12} m/Pa with a standard deviation of 0.49×10^{-12} m/Pa, which underestimates the true value (1×10^{-11} m/Pa). This is mainly because of the overestimation of amplitudes of the Born approximation in this frequency range (Appendix A).

For P-SV wavefield, the new LSM is applied to estimate η_T , assuming η_N to be zero. Similar to the SH wavefield, the initial gradient using P-SV wavefield (Figure 5c) contains strong artefacts, which are suppressed in the final LSM image (Figure 5d). Note that the results for the P-SV wavefield (Figure 5c and 5d) show an X shaped image, indicating the ambiguity in the fracture location; due to the source–receiver configuration, a fracture with the same dip angle but opposite sign would generate the same reflections. This ambiguity does not appear in the SH image (Figure 5a and 5b) because the Born operator \mathbf{L} including information of the fracture dip angle acts as a filter to suppress the artefacts. However, in the case of P-SV wavefield, they are not effectively suppressed due to the lack of a vertical component receiver. Note that these artefacts can be effectively removed by separately processing upgoing and downgoing waves (e.g., Hornby, 1989).

LABORATORY EXPERIMENT

Data

In this section, we apply the newly proposed LSM to laboratory experimental data. The laboratory experiments were performed in order to measure PP reflections from a horizontal fracture (Minato et al., 2018). An artificial fracture was created by installing spacers of 100 μm thickness between two aluminum blocks (Figure 6a). Vertical component reflection re-

sponses were measured for three different fracture conditions; dry fracture (i.e., the fracture is filled with air), homogeneously wet fracture (i.e., the fracture is filled with water), and heterogeneously wet fracture (i.e., the fracture is partly filled with water and partly with air). For each fracture condition, the location of source and receiver (piezo-electric transducers) was fixed so that the coupling condition between the surface of the sample and the transducers did not vary during the measurements. In total, 21 shot gathers were acquired; each shot gather contained on average 20 traces (Figure 6b). The observed PP reflections were isolated by time-windowing the data (Figure 6c). The measured response shows a center frequency of 700 KHz (Figure 6d). A more detailed measurement procedure can be found in Minato et al. (2018). In this study, we assume 2D wave propagation. Therefore, all observed data are scaled by \sqrt{t} in order to account for the difference in geometrical spreading between 3D and 2D wave propagation.

We first check the accuracy of the Born approximation in the configuration of the laboratory experiments; we numerically model the vertical component, zero-offset reflection response due to a vertical force source and a horizontal fracture located at the same depth as in the laboratory experiments (Figure 7). The input fracture compliances are $\eta_T = 1 \times 10^{-12}$ m/Pa and $\eta_N = 10 \times 10^{-14}$ m/Pa, respectively, considering a water-filled fracture without contact asperities and the results of an earlier AVO inversion using the same experimental data (Minato et al., 2018). Because of the large compliance values and the high center frequency, the Born approximation in this configuration is accurate only for very low-frequency components (lower than 200 KHz, Figure 7). Since high-resolution imaging requires large bandwidth and the signal-to-noise ratio is high around the center frequency of the measured responses, we use the frequency components between 50 KHz and 500 KHz for the proposed LSM.

Data calibration

To apply the proposed LSM, we estimate the source wavelets. Similar to previous AVO inversion (Minato and Ghose, 2016a; Minato et al., 2018), we use the dry fracture response in order to estimate the wavelets.

We first calculate theoretical dry fracture responses as follows. The dry fracture responses are considered to be free-surface reflections because the fracture does not contain contact asperities (Minato and Ghose, 2016a). We calculate the free-surface reflections in a homogeneous half space using the Kirchhoff approximation. Once we have calculated the theoretical PP reflection responses at the receiver positions, we introduce the additional effect of the free-surface boundary at the receiver; this is achieved by multiplying the calculated particle velocities by a factor of two, assuming normal-incidence reflections.

Next, we estimate the source wavelets by deconvolving the measured dry responses with the theoretical responses. We estimate the source wavelet at each trace (i.e., for each source–receiver pair) assuming that (1) for each source–receiver pair the source wavelet remains the same for different fracture conditions (dry and wet) due to the invariant coupling condition during the measurements, and (2) the source wavelets at each trace effectively account for complex source directivity at the transducers. The implementation of independent source wavelets at each source–receiver pair is straightforward in the Born operator \mathbf{L} in LSM (equations 9 and 14).

Imaging results

We apply the proposed LSM (equation 10) on a dataset representing a homogeneously wet fracture, assuming a 2D P-SV wavefield. The imaging area around the fracture ($0.3 \text{ m} \times$

0.05 m) is discretized with a spatial sampling interval of 0.5 mm. We image the normal fracture compliance η_N using only vertical component records. To this end, the tangential compliance is assumed (1×10^{-12} m/Pa) at the known fracture geometry, and the contribution of the tangential compliance in the vertical component records is subtracted from the measured data, assuming the Born approximation (equation 13 with $\Delta \mathbf{H}^b$ including only η_T). Finally, we formulate equation 9 where \mathbf{d} consists of the measured data, and \mathbf{m} the spatial distribution of η_N . The Born operator \mathbf{L} is calculated using free-space Green's functions and the estimated source wavelets.

As discussed earlier, we use the frequency components between 50 KHz and 500 KHz to obtain the result of LSM (Figure 8a). The final LSM image (Figure 8a) shows improved resolution than the initial gradient (Figure 8b). The initial gradient shows strong oscillations around the fracture due to the crosscorrelation of bandpass filtered data using a boxcar function; the LSM removes the effect of the source wavelet and suppresses artefacts that produce non-physical reflections.

Next, we quantitatively check the estimated fracture compliances. Figure 8c shows the estimated compliance of the homogeneously wet fracture along the fracture. The filled circles in Figure 8c show the fracture compliance obtained by AVO inversion, using the same dataset (Minato et al., 2018). The estimated fracture compliances using both approaches are similar. The LSM estimates smaller compliances than AVO inversion. Due to the over-estimation of the amplitudes in the Born approximation (see Figure 7), LSM underestimates the fracture compliances.

Finally, the proposed LSM is applied to the heterogeneously wet fracture responses (Figure 9). The procedure to construct the Born operator and to subtract the contribution

of the tangential compliance is the same as for the homogeneously wet fracture. As discussed earlier, the dry fracture responses are free-surface reflections, which correspond to responses due to infinitely large fracture compliances (Schoenberg, 1980). In this case, the Born approximation is not accurate to estimate the fracture compliances at the dry part of the fracture. Therefore, in Figure 9, the scaling effect due to the band-limited singular function is estimated at a representative location at the wet region. The result of LSM (Figure 9) clearly shows the difference between the wet region ($x = 0 \text{ m} - 0.15 \text{ m}$) and the dry region ($x = 0.15 \text{ m} - 0.30 \text{ m}$) along the fracture. The dry region of the fracture shows the magnitude of positive amplitudes similar to the negative amplitudes across the fracture (e.g., see the variation of the amplitudes at $x = 0.2 \text{ m}$ in Figure 9): the asymmetric amplitude variation across the fracture is not represented by the band-limited singular function with a unit spectrum between the minimum and maximum wavenumbers (equation B-2). This indicates that we cannot interpret the results at the dry region of the fracture as the singular function (equation B-2) scaled by the fracture compliance. In other words, the Born approximation fails to represent the dry part of the fracture as a nonwelded interface due to infinitely large compliances. We conclude that the proposed LSM successfully estimates the compliances of the wet fracture and also detects correctly the spatial variation in fracture compliances.

DISCUSSION

Frequency, accuracy, and resolution of LSM

We show numerically that the Born approximation of scattered waves due to linear-slip interfaces is generally accurate at low frequencies (Appendix C and Figure 7). Considering that LSM estimates the band-limited singular function (Dirac delta function) scaled by the

fracture compliances, large bandwidth data including high frequencies are necessary to obtain higher resolution images. However, including higher frequency components leads to an underestimation of the fracture compliances. This is because the Born approximation overpredicts the amplitudes, as discussed in the numerical modeling example. Therefore, there is a trade-off between the accuracy of the estimated compliance and the imaging resolution. Checking numerically the accuracy of the Born approximation at different frequencies is recommended to determine the frequency components to be used for LSM.

Feasibility of LSM using dipole acoustic logging

In the numerical modeling section, we show the application of the proposed LSM to the dipole acoustic measurements with a number of assumptions. First of all, we separately consider P-SV and SH wavefields, assuming wave propagation in the plane formed by the borehole axis and the normal vector of the fracture. Therefore, data acquisition requires the knowledge of the azimuth angle of the target fracture. However, when the azimuth angle of the fracture is not known, the rotation of the cross-dipole data (Lee et al., 2019) will be able to provide the input data for the proposed LSM and the azimuth angle of the target fracture.

Next, in the numerical modeling, we ignore the presence of the fluid-filled borehole. In this vein, the Born approximation for perturbations in Lamé constants in the borehole environment ignoring the borehole effect was investigated earlier (Geerits et al., 2013). However, a theoretical study shows that the fluid-filled borehole affects the radiation pattern at the source and the reception pattern at the receiver, especially at high frequencies (Tang et al., 2014). Angle- and frequency-dependent effects of the fluid-filled borehole on the source

radiation and receiver reception pattern can be implemented in the linearized equation 9 when the angle of the incident wave from the source and the angle of the scattered waves at the receiver can be appropriately calculated.

Complex geology

In the numerical modeling examples, we show that the proposed LSM is successfully applied to data with noise in simple configurations; reflection data due to a single horizontal fracture embedded in a homogeneous medium contaminated by random noise (the subsection “Laboratory-scale fracture imaging: numerical tests”) and data due to a single dipping fracture contaminated by scattered waves generated by a random background velocity field (the subsection “Borehole acoustic logging: numerical tests”). Imaging multiple fractures is possible without any modification because the proposed LSM estimates the spatial distribution of the fracture compliances (equation 14). In the boundary integral equation (Wapenaar, 2007), fractures may intersect each other. In this case, however, fracture compliances at the intersection may not be uniquely estimated using LSM because of the ambiguity regarding the fracture normal vector.

We use free-space Green’s functions in a homogeneous medium to calculate wave propagation in a background medium. However, any other approach which can handle a more complex background model (for example, smooth velocity variation and/or a layered earth model) can be used, e.g., using ray approximation, one-way wave equation, or finite-difference method (e.g., Operto et al., 2000; Kühn and Sacchi, 2003; Dai et al., 2010). When data contain reflections from both welded interfaces (geological layer boundaries) and nonwelded interfaces (fractures), there are two options: (1) explicitly incorporating welded

interfaces in the background velocity model and inverting only for the fracture compliances, or (2) simultaneously inverting for perturbations in elastic constants and fracture compliances. The former option requires prior knowledge of geological layer boundaries (e.g., from standard sonic logging in the case of single-well reflection imaging). The latter requires the modification of the Born operator (equation 13) to include scattering due to the perturbation in Lamé constants and density with respect to the background, which is represented by an additional volume integral (Beydoun and Mendes, 1989; Wapenaar, 2007).

Dip angle of a fracture

We assume that the dip angle of the fracture is known in the Born operator. The dip angles are assigned at each imaging grid point. The information of dip angles can be obtained from borehole images and/or standard migration images. Alternatively, it is possible to include dip angles or a vector normal to the fracture (n_x and n_z) in the inversion parameters of LSM. In this case, however, LSM estimates the indirect parameters which couple the fracture compliances and the normal vector (see the components of the contrast function $\Delta\mathbf{H}^b$ in equation A-12). Note that, in this case, at least two additional unknown parameters are involved in the inversion, which is computationally more expensive.

CONCLUSION

In this study, we propose a new elastic least-squares migration method for thin compliant zones (fractures, joints and faults) in order to estimate the fracture compliance tensor with high resolution. We derive the Born approximation in order to linearize the scattered wavefield with respect to the fracture compliances. We consider a 2D wave propagation

problem, i.e., P-SV and SH wavefields.

We show two numerical examples of the new LSM: laboratory-scale fracture imaging and field-scale fracture imaging using borehole acoustic logging data. The LSM generally provides images with higher resolution than the initial gradient or the image with classical crosscorrelation imaging condition. Furthermore, an anisotropic fracture with non-zero coupling compliance is imaged much better by the new LSM than by the conventional LSM where the perturbation of Lamé constants is estimated. This indicates that the new LSM is essential in accurate imaging of rough fractures, where shear-induced coupling changes are monitored. The dipole acoustic input data are modeled considering a random background medium. The results show the potential of the new LSM to provide quantitative imaging of fracture compliances of a dipping fracture embedded in a complex background medium.

Finally, we apply the new LSM to a laboratory experimental dataset. The estimated compliance values are similar to those obtained by AVO inversion. The compliance values are, however, underestimated because at higher frequencies the Born approximation overpredicts the amplitudes. The LSM image detects a spatially varying fracture condition resulting from the partial inclusion of water in the fracture.

The linear-slip theory and the fracture compliance tensor describe the interaction between the seismic waves and the compliant zones with an effective thickness that is much smaller than the seismic wavelength. Quantitatively imaging the fracture compliance tensor is, therefore, crucial to further address the small-scale properties at fractures, joints and geological faults.

ACKNOWLEDGMENTS

The authors thank editors and reviewer A. Stovas, and three anonymous reviewers for their comments and suggestions that improved the paper. The research of K. Wapenaar has received funding from the European Research Council (ERC) under the European Union's Horizon 2020 research and innovation program (grant no. 742703).

APPENDIX A

LINEAR-SLIP BOUNDARY CONDITION AND REPRESENTATION THEOREM IN A 2D PROBLEM

P-SV wavefield

We explicitly formulate vectors and matrices necessary to define the linear-slip boundary condition (equation 5) and the boundary integral representation (equation 12 and 13) for 2D P-SV wavefield.

The wave vector \mathbf{u} is

$$\mathbf{u} = \begin{pmatrix} v_x \\ v_z \\ -\tau_{xx} \\ -\tau_{zz} \\ -\tau_{xz} \end{pmatrix}. \quad (\text{A-1})$$

Similar to 3D problem (see the main text), \mathbf{Y} (a 5×5 matrix) in equation 5 can be written for a linear-slip interface with an arbitrary dip angle using the fracture compliance tensor of a horizontal fracture $\boldsymbol{\eta}_h$. We obtain an equation with the same form as equation

8, but $\boldsymbol{\eta}_h$ defined as,

$$\boldsymbol{\eta}_h = \begin{pmatrix} \eta_{T_1} & \eta_C \\ \eta_C & \eta_N \end{pmatrix}, \quad (\text{A-2})$$

and $\mathbf{Q} = \begin{pmatrix} n_z & -n_x \\ n_x & n_z \end{pmatrix}$. For completeness, a 4×5 matrix \mathbf{M} in equation 5 is defined as,

$$\mathbf{M} = \begin{pmatrix} 1 & 0 & 0 & 0 & 0 \\ 0 & 1 & 0 & 0 & 0 \\ 0 & 0 & n_x & 0 & n_z \\ 0 & 0 & 0 & n_z & n_x \end{pmatrix}. \quad (\text{A-3})$$

The Green's matrix \mathbf{G} consists of Green's functions in P-SV wavefield, defined as

$$\mathbf{G} = \begin{pmatrix} G_{x,x}^{v,f} & G_{x,z}^{v,f} & G_{x,xx}^{v,h} & G_{x,zz}^{v,h} & G_{x,xz}^{v,h} \\ G_{z,x}^{v,f} & G_{z,z}^{v,f} & G_{z,xx}^{v,h} & G_{z,zz}^{v,h} & G_{z,xz}^{v,h} \\ G_{xx,x}^{\tau,f} & G_{xx,z}^{\tau,f} & G_{xx,xx}^{\tau,h} & G_{xx,zz}^{\tau,h} & G_{xx,xz}^{\tau,h} \\ G_{zz,x}^{\tau,f} & G_{zz,z}^{\tau,f} & G_{zz,xx}^{\tau,h} & G_{zz,zz}^{\tau,h} & G_{zz,xz}^{\tau,h} \\ G_{xz,x}^{\tau,f} & G_{xz,z}^{\tau,f} & G_{xz,xx}^{\tau,h} & G_{xz,zz}^{\tau,h} & G_{xz,xz}^{\tau,h} \end{pmatrix}, \quad (\text{A-4})$$

where the superscripts of the Green's functions represent the type of the observed wavefield (e.g., particle velocity (v) or stress (τ)) and the type of source (e.g., force (f) or deformation rate (h)), and the subscripts represent the different components. Please see Wapenaar (2007) for more details on the notation in the case of an acoustic wavefield, and Wapenaar and Fokkema (2004) for more details in the definitions of the source types in the case of an elastodynamic wavefield.

The contrast function $\Delta \mathbf{H}^b$ in the boundary integral representation (equation 12) can be derived from equation 56 in Wapenaar (2007) using \mathbf{M} (equation A-3), \mathbf{Y} (equation 8 but using $\boldsymbol{\eta}_h$ and \mathbf{Q} defined in this subsection), $\mathbf{K} = \text{diag}(1, 1, -1, -1, -1)$, and $\mathbf{N} = \begin{pmatrix} \mathbf{0} & \mathbf{I} \\ -\mathbf{I} & \mathbf{0} \end{pmatrix}$.

Finally, we obtain,

$$\Delta \mathbf{H}^b = j\omega \begin{pmatrix} 0 & 0 & 0 & 0 & 0 \\ 0 & 0 & 0 & 0 & 0 \\ 0 & 0 & & & \\ 0 & 0 & \mathbf{M}_1^T \mathbf{Q}^T \Delta \boldsymbol{\eta}_h \mathbf{Q} \mathbf{M}_1 & & \\ 0 & 0 & & & \end{pmatrix}, \quad (\text{A-5})$$

where

$$\mathbf{M}_1 = \begin{pmatrix} n_x & 0 & n_z \\ 0 & n_z & n_x \end{pmatrix}, \quad (\text{A-6})$$

and

$$\Delta \boldsymbol{\eta}_h = \begin{pmatrix} \Delta \eta_{T_1} & \Delta \eta_C \\ \Delta \eta_C & \Delta \eta_N \end{pmatrix}. \quad (\text{A-7})$$

The symbol Δ in equation A-7 denotes the difference in the fracture compliances between the reference medium and the actual medium. When the reference medium does not contain fractures (fracture compliances are 0), $\Delta \boldsymbol{\eta}_h$ is equivalent to $\boldsymbol{\eta}_h$.

SH wavefield

In case of a 2D SH wavefield, the wave vector \mathbf{u} is

$$\mathbf{u} = \begin{pmatrix} v_y \\ -\tau_{xy} \\ -\tau_{yz} \end{pmatrix}. \quad (\text{A-8})$$

The fracture compliance tensor becomes a scalar, η_{T_2} (see equation 4). The linear-slip boundary condition is represented by equation 5 using \mathbf{M} and \mathbf{Y} defined as,

$$\mathbf{M} = \begin{pmatrix} 1 & 0 & 0 \\ 0 & n_x & n_z \end{pmatrix}, \quad (\text{A-9})$$

and

$$\mathbf{Y} = \begin{pmatrix} 0 & \eta_{T_2} \\ 0 & 0 \end{pmatrix}. \quad (\text{A-10})$$

The Green's matrix is

$$\mathbf{G} = \begin{pmatrix} G_{y,y}^{v,f} & G_{y,xy}^{v,h} & G_{y,yz}^{v,h} \\ G_{xy,y}^{\tau,f} & G_{xy,xy}^{\tau,h} & G_{xy,yz}^{\tau,h} \\ G_{yz,y}^{\tau,f} & G_{yz,xy}^{\tau,h} & G_{yz,yz}^{\tau,h} \end{pmatrix}. \quad (\text{A-11})$$

Similar to P-SV wavefield, the contrast function $\Delta\mathbf{H}^b$ in the boundary integral representation (equation 12) can be derived from equation 56 in Wapenaar (2007) using \mathbf{M} (equation A-9), \mathbf{Y} (equation A-10), $\mathbf{K} = \text{diag}(1, -1, -1)$, and $\mathbf{N} = \begin{pmatrix} 0 & 1 \\ -1 & 0 \end{pmatrix}$. Finally, we obtain,

$$\Delta\mathbf{H}^b = j\omega \begin{pmatrix} 0 & 0 & 0 \\ 0 & n_x^2 \Delta\eta_{T_2} & n_x n_z \Delta\eta_{T_2} \\ 0 & n_x n_z \Delta\eta_{T_2} & n_z^2 \Delta\eta_{T_2} \end{pmatrix}, \quad (\text{A-12})$$

where $\Delta\eta_{T_2}$ denotes the difference in the tangential fracture compliance between the reference medium and the actual medium. When the reference medium does not contain fractures, $\Delta\eta_{T_2}$ is η_{T_2} .

APPENDIX B

COMPENSATION OF THE SCALING EFFECT DUE TO THE BAND-LIMITED SINGULAR FUNCTION

In this study, LSM estimates the band-limited singular function scaled by the fracture compliances (equation 14). The output image of LSM, therefore, includes the scaling effect

of the band-limited singular function; we compensate for it by estimating the bandwidth of the output image.

We consider that the fracture geometry ∂D_{int} is described parametrically in terms of one parameter s , i.e., $x = x(s)$ and $z = z(s)$. In this case, the singular function δ_{Σ} in equation 14 has the following property:

$$\int_{\mathcal{V}} \delta_{\Sigma}(x, z) f(x, z) dx dz = \int_{\partial D_{\text{int}}} f(x(s), z(s)) ds, \quad (\text{B-1})$$

where $f(x, z)$ is a test function. For brevity, in this appendix, we consider a horizontal fracture located at $z = 0$. In this case, $\delta_{\Sigma}(x, z) = \delta(z)$, where $\delta(z)$ is the Dirac delta function. We assume that the band-limited Dirac delta function, $\tilde{\delta}(z)$, in the result of LSM, is approximated by an unit spectrum in the wavenumber domain parametrized by the maximum wavenumber (L_k) and the minimum wavenumber (l_k),

$$\tilde{\delta}(z) = \frac{L_k \sin(L_k z)}{\pi L_k z} - \frac{l_k \sin(l_k z)}{\pi l_k z}. \quad (\text{B-2})$$

Once we have estimated L_k and l_k , the output image of LSM is scaled so that the maximum amplitude of $\tilde{\delta}(z)$ becomes 1.

In this study, we estimate L_k and l_k of the output image of LSM as follows: (1) we first solve the linearized inversion (LSM) and obtain $m(x, z)$, where we replace the vector representation of the model parameter \mathbf{m} in equation 9 by its spatial distribution $m(x, z)$, (2) we extract an one-dimensional amplitude distribution of m normal to the fracture (in the case of a horizontal fracture, we extract $m(x_0, z)$ where x_0 is a fixed lateral position), and (3) we estimate L_k and l_k either in the wavenumber domain by reading the minimum and maximum wavenumbers or in the space domain by fitting $m(x_0, z)$ using equation B-2. In this study, we use the latter approach for estimating L_k and l_k . To this end, we first normalize the amplitude of $m(x_0, z)$, and we search for L_k and l_k which best fit $m(x_0, z)$

using equation B-2 whose amplitudes are also normalized. Figure B-1a shows an example of the estimation of L_k and l_k for the numerical example of Figure 2b. As expected from equation B-2, the estimated amplitude distribution, $m(0.15, z)$, is symmetric around the fracture location ($z = 0.172$ m). The best fit curve (black line in Figure B-1a) is obtained by using $L_k = 543.50$ (rad) and $l_k = 40.84$ (rad), respectively. The Fourier spectrum (Figure B-1b) shows that we successfully estimated L_k and l_k . The output image of LSM is then scaled by $(L_k/\pi - l_k/\pi)^{-1}$, and we obtain the result shown in Figure 2b. Note that for a dipping fracture, we evaluate the spatial distribution of $m(x, z)$ along the perpendicular direction of the imaged fracture.

APPENDIX C

ACCURACY OF BORN APPROXIMATION IN NUMERICAL EXAMPLES

In this appendix, we show the accuracy of the Born approximation (equation 13) in the configurations of the numerical modeling section.

We first consider the numerical modeling of laboratory-scale measurements (Figure 1a), where we model zero-offset reflection responses. Figure C-1 shows the comparison between the Born approximated response ('Born') and the true response ('Total'). The true response is calculated using the wavenumber domain method (Nakagawa et al., 2004). Figures C-1a–C-1c are the frequency spectra of modeled Green's functions for SH wavefield (v_y) and P-SV wavefield (v_z and v_x). Figures C-1d–C-1f show the time-domain waveforms after the convolution of a Ricker wavelet (50 KHz center frequency) with the modeled Green's functions. For this particular model, the Born approximation is accurate at low frequencies (lower

than 200 KHz). At higher frequencies the Born approximation overpredicts amplitudes.

Next, we consider the configuration in the dipole acoustic measurements (Figure 4a). For simplicity, we assume a homogeneous background medium with the average P and S wave velocities of the random model (Figure 4a), and we calculate zero-offset reflection responses due to a horizontal fracture located at 5 m distance from the source and receiver. The dipole sources are modeled as point force sources parallel to the fracture. Similar to Figure C-1, Figures C-2a and C-2b are the frequency spectra of modeled Green's functions, and Figures C-2c–C-2d show the time-domain waveforms after the convolution of a Ricker wavelet (3 KHz center frequency) with the modeled Green's functions. Contrary to Figures C-1a–C-1c, the frequencies where the Born approximation is accurate for this configuration are very low (lower than 3 KHz, Figures C-2a and C-2b). This is because the order of magnitude of fracture compliances in the field-scale fracture ($\eta_T = 1 \times 10^{-11}$ m/Pa, $\eta_N = 1 \times 10^{-12}$ m/Pa) is larger than that of the laboratory-scale fracture ($\eta_T = 4.5 \times 10^{-14}$ m/Pa, $\eta_N = 1.75 \times 10^{-14}$ m/Pa, $\eta_C = 1.40 \times 10^{-14}$ m/Pa).

REFERENCES

- Aydin, A., 2000, Fractures, faults, and hydrocarbon entrapment, migration and flow: *Marine and Petroleum Geology*, **17**, 797–814, doi: 10.1016/S0264-8172(00)00020-9.
- Bakulin, A., V. Grechka, and I. Tsvankin, 2000a, Estimation of fracture parameters from reflection seismic data—Part I: HTI model due to a single fracture set: *Geophysics*, **65**, 1788–1802, doi: 10.1190/1.1444863.
- , 2000b, Estimation of fracture parameters from reflection seismic data—Part II: Fractured models with orthorhombic symmetry: *Geophysics*, **65**, 1803–1817, doi: 10.1190/1.1444864.
- Barbosa, N. D., E. Caspari, J. G. Rubino, A. Greenwood, L. Baron, and K. Holliger, 2019, Estimation of fracture compliance from attenuation and velocity analysis of full-waveform sonic log data: *Journal of Geophysical Research: Solid Earth*, **124**, 2738–2761, doi: 10.1029/2018JB016507.
- Barbosa, N. D., J. G. Rubino, E. Caspari, and K. Holliger, 2017, Extension of the classical linear slip model for fluid-saturated fractures: Accounting for fluid pressure diffusion effects: *Journal of Geophysical Research: Solid Earth*, **122**, 1302–1323, doi: 10.1002/2016JB013636.
- Ben-Zion, Y., and C. Sammis, 2003, Characterization of fault zones: *Pure and Applied Geophysics*, **160**, 677–715, doi: 10.1007/PL00012554.
- Beydoun, W. B., and M. Mendes, 1989, Elastic ray-Born L2-migration/inversion: *Geophysical Journal International*, **97**, 151–160, doi: 10.1111/j.1365-246X.1989.tb00490.x.
- Bleistein, N., 1987, On the imaging of reflectors in the earth: *Geophysics*, **52**, 931–942, doi: 10.1190/1.1442363.
- Bostock, M., 2002, Kirchhoff-approximate inversion of teleseismic wavefields: *Geophysical*

- Journal International, **149**, 787–795, doi: 10.1046/j.1365-246X.2002.01687.x.
- Chen, K., and M. D. Sacchi, 2017, Elastic least-squares reverse time migration via linearized elastic full-waveform inversion with pseudo-Hessian preconditioning: *Geophysics*, no. 5, **82**, S341–S358, doi: 10.1190/geo2016-0613.1.
- Cheng, C. C., and M. Sansalone, 1995, Determining the minimum crack width that can be detected using the impulse-echo method Part 1: Experimental study: *Materials and Structures*, **28**, 74–82, doi: 10.1007/BF02473174.
- Claerbout, J. F., 1971, Toward a unified theory of reflector mapping: *Geophysics*, **36**, 467–481, doi: 10.1190/1.1440185.
- Coates, R., and M. Schoenberg, 1995, Finite difference modeling of faults and fractures: *Geophysics*, **60**, 1514–1526, doi: 10.1190/1.1443884.
- Crampin, S., 1984, Effective anisotropic elastic constants for wave propagation through cracked solids: *Geophysical Journal International*, **76**, 135–145, doi: 10.1111/j.1365-246X.1984.tb05029.x.
- Cui, X., E. S. Krebs, and L. R. Lines, 2017, Seismic inversion for geologic fractures and fractured media: *Geophysics*, **82**, no. 5, C145–C161, doi: 10.1190/geo2016-0123.1.
- Dai, W., C. Boonyasiriwat, and G. T. Schuster, 2010, 3D multi-source least-squares reverse time migration: 80th Annual International Meeting, SEG, Expanded Abstracts, 3120–3124, doi: 10.1190/1.3513494.
- Dai, W., X. Wang, and G. T. Schuster, 2011, Least-squares migration of multisource data with a deblurring filter: *Geophysics*, **76**, no. 5, R135–R146, doi: 10.1190/geo2010-0159.1.
- de Hoop, A. T., 1995, *Handbook of radiation and scattering of waves*: Academic Press, .
- Far, M. E., L. Thomsen, and C. M. Sayers, 2013, Seismic characterization of reservoirs with asymmetric fractures: *Geophysics*, **78**, no. 2 , N1–N10, doi: 10.1190/geo2012-0319.1.

- Feng, Z., and G. T. Schuster, 2017, Elastic least-squares reverse time migration: *Geophysics*, **82**, no. 2, S143–S157, doi: 10.1190/geo2016-0254.1.
- Fossen, H., R. A. Schultz, Z. K. Shipton, and K. Mair, 2007, Deformation bands in sandstone: a review: *Journal of the Geological Society*, **164**, 755–769, doi: 10.1144/0016-76492006-036.
- Geerits, T. W., I. Veile, and O. Hellwig, 2013, Far field elastodynamic Born scattering revisited: *Journal of Applied Geophysics*, **89**, 141–163, doi: 10.1016/j.jappgeo.2012.11.012.
- Gong, H., H. Chen, X. He, C. Su, X. M. Wang, B. C. Wang, and X. H. Yan, 2018, Modeling and inversions of acoustic reflection logging imaging using the combined monopole–dipole measurement mode: *Applied Geophysics*, **15**, 393–400, doi: 10.1007/s11770-018-0700-y.
- Hardin, E., C. H. Cheng, F. L. Paillet, and J. D. Mendelson, 1987, Fracture characterization by means of attenuation and generation of tube waves in fractured crystalline rock at Mirror Lake, New Hampshire: *Journal of Geophysical Research*, **92**, 7989–8006, doi: 10.1029/JB092iB08p07989.
- Hobday, C., and M. Worthington, 2012, Field measurements of normal and shear fracture compliance: *Geophysical Prospecting*, **60**, 488–499, doi: 10.1111/j.1365-2478.2011.01000.x.
- Hornby, B., D. Johnson, K. Winkler, and R. Plumb, 1989, Fracture evaluation using reflected Stoneley-wave arrivals: *Geophysics*, **54**, 1274–1288, doi: 10.1190/1.1442587.
- Hornby, B. E., 1989, Imaging of near-borehole structure using full-waveform sonic data: *Geophysics*, **54**, 747–757, doi: 10.1190/1.1442702.
- Huang, Y., and G. T. Schuster, 2012, Multisource least-squares migration of marine streamer and land data with frequency-division encoding: *Geophysical Prospecting*, **60**, 663–680, doi: 10.1111/j.1365-2478.2012.01086.x.

- Jin, S., R. Madariaga, J. Virieux, and G. Lambaré, 1992, Two-dimensional asymptotic iterative elastic inversion: *Geophysical Journal International*, **108**, 575–588, doi: 10.1111/j.1365-246X.1992.tb04637.x.
- Kame, N., K. Nagata, M. Nakatani, and T. Kusakabe, 2014, Feasibility of acoustic monitoring of strength drop precursory to earthquake occurrence: *Earth, Planets and Space*, **66**, 1–12, doi: 10.1186/1880-5981-66-41.
- Kühl, H., and M. D. Sacchi, 2003, Least-squares wave-equation migration for AVP/AVA inversion: *Geophysics*, **68**, 262–273, doi: 10.1190/1.1543212.
- Lambaré, G., J. Virieux, R. Madariaga, and S. Jin, 1992, Iterative asymptotic inversion in the acoustic approximation: *Geophysics*, **57**, 1138–1154, doi: 10.1190/1.1443328.
- Leary, P. C., S. Crampin, and T. V. McEvelly, 1990, Seismic fracture anisotropy in the earth's crust: An overview: *Journal of Geophysical Research: Solid Earth*, **95**, 11105–11114, doi: 10.1029/JB095iB07p11105.
- Lee, S. Q., X. M. Tang, and Y. D. Su, 2019, Shear wave imaging to determine near-borehole faults for ocean drilling exploration: *Geophysical Journal International*, **217**, 288–293, doi: 10.1093/gji/ggz023.
- Li, C., and W. Yue, 2015, High-resolution adaptive beamforming for borehole acoustic reflection imaging: *Geophysics*, **80**, no. 6, D565–D574, doi: 10.1190/geo2014-0517.1.
- Li, J., K. A. Innanen, and G. Tao, 2017, Extraction of reflected events from sonic-log waveforms using the Karhunen-Loève transform: *Geophysics*, **82**, no. 5, D265–D277, doi: 10.1190/geo2017-0031.1.
- Li, J., H. Li, Y. Jiao, Y. Liu, X. Xia, and C. Yu, 2014a, Analysis for oblique wave propagation across filled joints based on thin-layer interface model: *Journal of Applied Geophysics*, **102**, 39–46, doi: 10.1016/j.jappgeo.2013.11.014.

- Li, J., G. Tao, K. Zhang, B. Wang, and H. Wang, 2014b, An effective data processing flow for the acoustic reflection image logging: *Geophysical Prospecting*, **62**, 530–539, doi: 10.1111/1365-2478.12103.
- Liu, E., and A. Martinez, 2013, *Seismic fracture characterization: Concepts and practical applications*: EAGE Publications BV.
- Lubbe, R., J. Sothcott, M. Worthington, and C. McCann, 2008, Laboratory estimates of normal and shear fracture compliance: *Geophysical Prospecting*, **56**, 239–247, doi: 10.1111/j.1365-2478.2007.00688.x.
- Menke, W., 1989, *Geophysical data analysis: discrete inverse theory*: Academic Press.
- Minato, S., and R. Ghose, 2014, Imaging and characterization of a subhorizontal non-welded interface from point source elastic scattering response: *Geophysical Journal International*, **197**, 1090–1095, doi: 10.1093/gji/ggu037.
- , 2016a, AVO inversion for a non-welded interface: estimating compliances of a fluid-filled fracture: *Geophysical Journal International*, **206**, 56–62, doi: 10.1093/gji/ggw138.
- , 2016b, Enhanced characterization of fracture compliance heterogeneity using multiple reflections and data-driven Green’s function retrieval: *Journal of Geophysical Research: Solid Earth*, **121**, 2813–2836, doi: 10.1002/2015JB012587.
- Minato, S., R. Ghose, and G. Osukuku, 2018, Experimental verification of spatially varying fracture-compliance estimates obtained from amplitude variation with offset inversion coupled with linear slip theory: *Geophysics*, **83**, no. 1, WA1–WA8, doi: 10.1190/geo2017-0069.1.
- Minato, S., R. Ghose, T. Tsuji, M. Ikeda, and K. Onishi, 2017, Hydraulic properties of closely spaced dipping open fractures intersecting a fluid-filled borehole derived from tube wave generation and scattering: *Journal of Geophysical Research: Solid Earth*,

- 122**, 8003–8020, doi: 10.1002/2017JB014681.
- Nagy, P., 1992, Ultrasonic classification of imperfect interfaces: *Journal of Nondestructive Evaluation*, **11**, 127–139, doi: 10.1007/BF00566404.
- Nakagawa, S., K. Nihei, and L. Myer, 2000, Shear-induced conversion of seismic waves across single fractures: *International Journal of Rock Mechanics and Mining Sciences*, **37**, 203–218, doi: 10.1016/S1365-1609(99)00101-X.
- Nakagawa, S., K. T. Nihei, and L. R. Myer, 2004, Plane wave solution for elastic wave scattering by a heterogeneous fracture: *The Journal of the Acoustical Society of America*, **115**, 2761–2772, doi: 10.1121/1.1739483.
- Nakagawa, S., and M. A. Schoenberg, 2007, Poroelastic modeling of seismic boundary conditions across a fracture: *The Journal of the Acoustical Society of America*, **122**, 831–847, doi: 10.1121/1.2747206.
- Nemeth, T., C. Wu, and G. T. Schuster, 1999, Least-squares migration of incomplete reflection data: *Geophysics*, **64**, 208–221, doi: 10.1190/1.1444517.
- Operto, M. S., S. Xu, and G. Lambaré, 2000, Can we quantitatively image complex structures with rays?: *Geophysics*, **65**, 1223–1238, doi: 10.1190/1.1444814.
- Palmer, S., J. Smith, and K. Waters, 1981, Fracture detection in crystalline rocks using ultrasonic reflection techniques: *International Journal of Rock Mechanics and Mining Sciences*, **18**, 403–413, doi: 10.1016/0148-9062(81)90004-8.
- Peng, S., Y. Lu, X. Cui, and W. Du, 2017, Seismic fracture AVO modeling and inversion: 79th Annual International Conference and Exhibition, EAGE, Extended Abstracts, 1–5, doi: 10.3997/2214-4609.201700829.
- Plessix, R. E., and W. Mulder, 2004, Frequency-domain finite-difference amplitude-preserving migration: *Geophysical Journal International*, **157**, 975–987, doi:

10.1111/j.1365-246X.2004.02282.x.

Pourahmadian, F., B. B. Guzina, and H. Haddar, 2017, A synoptic approach to the seismic sensing of heterogeneous fractures: From geometric reconstruction to interfacial characterization: *Computer Methods in Applied Mechanics and Engineering*, **324**, 395–412, doi: 10.1016/j.cma.2017.06.002.

Pyrak-Nolte, L., and D. Nolte, 1992, Frequency dependence of fracture stiffness: *Geophysical Research Letters*, **19**, 325–328, doi: 10.1029/91GL03179.

Reshetnikov, A., S. Buske, and S. Shapiro, 2010, Seismic imaging using microseismic events: Results from the San Andreas fault system at SAFOD: *Journal of Geophysical Research: Solid Earth*, **115**, doi: 10.1029/2009JB007049.

Rokhlin, S. I., and Y. J. Wang, 1991, Analysis of boundary conditions for elastic wave interaction with an interface between two solids: *The Journal of the Acoustical Society of America*, **89**, 503–515, doi: 10.1121/1.400374.

Saenger, E. H., and S. A. Shapiro, 2002, Effective velocities in fractured media: a numerical study using the rotated staggered finite-difference grid: *Geophysical Prospecting*, **50**, 183–194, doi: 10.1046/j.1365-2478.2002.00309.x.

Schoenberg, M., 1980, Elastic wave behavior across linear slip interfaces: *The Journal of the Acoustical Society of America*, **68**, 1516–1521, doi: 10.1121/1.385077.

Segall, P., and D. Pollard, 1980, Mechanics of discontinuous faults: *Journal of Geophysical Research: Solid Earth*, **85**, 4337–4350, doi: 10.1029/JB085iB08p04337.

Tang, Y., and B. Biondi, 2009, Least-squares migration/inversion of blended data: 79th Annual International Meeting, SEG, Expanded Abstracts, 2859–2863, doi: 10.1190/1.3255444.

Tang, X. M., J. J. Cao, and Z. T. Wei, 2014, Shear-wave radiation, reception, and reciprocity

- of a borehole dipole source: With application to modeling of shear-wave reflection survey: *Geophysics*, **79**, no. 2, T43–T50, doi: 10.1190/geo2013-0096.1.
- Tang, X. M., Z. Li, C. Hei, and Y. D. Su, 2016, Elastic wave scattering to characterize heterogeneities in the borehole environment: *Geophysical Journal International*, **205**, 594–603, doi: 10.1093/gji/ggw037.
- Tang, X. M., and D. J. Patterson, 2009, Single-well S-wave imaging using multicomponent dipole acoustic-log data: *Geophysics*, **74**, no. 6, WCA211–WCA223, doi: 10.1190/1.3227150.
- , 2010, Mapping formation radial shear-wave velocity variation by a constrained inversion of borehole flexural-wave dispersion data: *Geophysics*, **75**, no. 6, E183–E190, doi: 10.1190/1.3502664.
- Tarantola, A., 1984, Inversion of seismic reflection data in the acoustic approximation: *Geophysics*, **49**, 1259–1266, doi: 10.1190/1.1441754.
- Tura, A., C. Hanitzsch, and H. Calandra, 1998, 3-D AVO migration/inversion of field data: *The Leading Edge*, **17**, 1578–1578, doi: 10.1190/1.1437898.
- Wapenaar, K., 2007, General representations for wavefield modeling and inversion in geophysics: *Geophysics*, **72**, no. 5, SM5–SM17, doi: 10.1190/1.2750646.
- Wapenaar, K., and J. Fokkema, 2004, Reciprocity theorems for diffusion, flow, and waves: *A.S.M.E. Journal of Applied Mechanics*, **71**, 145–150, doi: 10.1115/1.1636792.
- Wapenaar, K., E. Slob, and J. Fokkema, 2004, Reciprocity and power balance for piecewise continuous media with imperfect interfaces: *Journal of Geophysical Research*, **109**, B10301, doi: 10.1029/2004JB003002.
- White, J. E., 1983, *Underground sound: Application of seismic waves*: Elsevier Amsterdam.
- Willis, M., D. Burns, R. Rao, B. Minsley, M. Toksöz, and L. Vetri, 2006, Spatial orientation

- and distribution of reservoir fractures from scattered seismic energy: *Geophysics*, **71**, no. 5, O43–O51, doi: 10.1190/1.2235977.
- Worthington, M. H., and J. A. Hudson, 2000, Fault properties from seismic Q: *Geophysical Journal International*, **143**, 937–944, doi: 10.1046/j.1365-246X.2000.00315.x.
- Worthington, M. H., 2007, The compliance of macrofractures: *The Leading Edge*, **26**, 1118–1122, doi: 10.1190/1.2780780.
- Wu, C., J. M. Harris, K. T. Nihei, and S. Nakagawa, 2005, Two-dimensional finite-difference seismic modeling of an open fluid-filled fracture: Comparison of thin-layer and linear-slip models: *Geophysics*, **70**, no. 4, T57–T62, doi: 10.1190/1.1988187.
- Wu, R. S., and K. Aki, 1985, Scattering characteristics of elastic waves by an elastic heterogeneity: *Geophysics*, **50**, 582–595, doi: 10.1190/1.1441934.
- Xu, S., H. Chauris, G. Lambaré, and M. Noble, 2001, Common-angle migration: A strategy for imaging complex media: *Geophysics*, **66**, 1877–1894, doi: 10.1190/1.1487131.
- Xu, S., Y. Zhang, and B. Tang, 2011, 3D angle gathers from reverse time migration: *Geophysics*, **76**, no. 2, S77–S92, doi: 10.1190/1.3536527.
- Yang, K., and J. Zhang, 2019, Comparison between Born and Kirchhoff operators for least-squares reverse time migration and the constraint of the propagation of the background wavefield: *Geophysics*, **84**, no. 5, R725–R739, doi: 10.1190/geo2018-0438.1.
- Yousef, B., and D. Angus, 2016, When do fractured media become seismically anisotropic? some implications on quantifying fracture properties: *Earth and Planetary Science Letters*, **444**, 150–159, doi: 10.1016/j.epsl.2016.03.040.

LIST OF FIGURES

1 (a) Configuration of numerical modeling. (b) Fracture compliances along the fracture. Tangential (η_T), normal (η_N) and coupling (η_C) compliances are shown. (c) Modeled shot gather showing SH wavefield. (d) Modeled shot gather for P-SV wavefield. (e) Calculated traveltimes of specular reflections. (f) Calculated traveltimes of non-specular reflections from the edges of the fracture. PPd: diffracted P wave due to incident P wave, PSd: diffracted S wave due to incident P wave, SPd: diffracted P wave due to incident S wave, and SSd: diffracted S wave due to incident S wave.

2 Imaging results for SH wavefield; (a) Initial gradient without inversion, (b) proposed LSM involving linear-slip theory, and (c) conventional LSM without linear-slip theory. (d) Residuals at each CG iteration using the proposed LSM and the conventional LSM.

3 Imaging results for P-SV wavefield using the proposed LSM; (a) tangential compliance, (b) normal compliance, and (c) coupling compliance. (d)–(e) Imaging results using the conventional LSM for the perturbation in λ and μ . (f) Residuals at each CG iteration using the proposed LSM and the conventional LSM.

4 (a) Configuration of borehole acoustic measurements. First and last source-receiver geometries and the background velocity model are shown. The red line indicates the fracture. The dotted line indicates the location of the borehole. (b) Numerically modeled dipole data (SH wavefield) at the first receiver due to varying source depths. (c) Same as (b) but for P-SV wavefield. (d) Calculated traveltimes of direct waves (P and S), Stoneley wave (St), and reflected waves from the fracture (PP, SS, PS and SP).

5 Imaging results using SH wavefield in dipole acoustic logging data; (a) Initial gradient without inversion, (b) the proposed LSM. (c),(d) Same as (a),(b) but using P-SV wavefield.

6 (a) Configuration of laboratory experiments. The fracture aperture is created using 100 μm thick spacers. (b) Source–receiver geometry for the measured data. (c) An example of the measured PP reflection data for a source located at 0.11 m. (d) Frequency spectrum of (c).

7 Frequency spectrum of the numerically modeled reflection response, representing the laboratory geometry and the fracture compliances. The total response and the Born approximation are shown.

8 (a) Imaging results on laboratory experimental data of a homogeneously wet fracture using the proposed LSM (50–500 KHz). (b) Imaging result using initial gradient. (c) Estimated normal fracture compliance along the fracture from the proposed LSM and the AVO inversion from Minato et al. (2018).

9 Imaging results on laboratory experimental data of a heterogeneously wet fracture using the proposed LSM (50–500 KHz).

B-1 (a) An example of the estimation of L_k and l_k in equation B-2. The red line shows the output of LSM at $x = 0.15$ m followed by normalization of the amplitude, and the black line shows the best-fit curve using equation B-2 with $(L_k, l_k) = (543.50, 40.84)$. (b) The Fourier spectrum of (a) and the detected values of L_k and l_k .

C-1 Born approximated response (Born) and true response (Total) for zero-offset record in the configuration of Figure 1a. (a),(b),(c) Modeled Green’s functions for SH wavefield (v_y) and P-SV wavefield (v_z and v_x). (d),(e),(f) Time-domain responses of (a),(b),(c) after convolution of Ricker wavelet with 50 KHz center frequency.

C-2 Born approximated response (Born) and true response (Total) for zero-offset record in the configuration of Figure 4a. (a),(b) Modeled Green’s functions for SH wavefield (v_y) and P-SV wavefield (v_x). (c),(d) Time-domain responses of (a),(b) after convolution of

Ricker wavelet with 3 KHz center frequency.

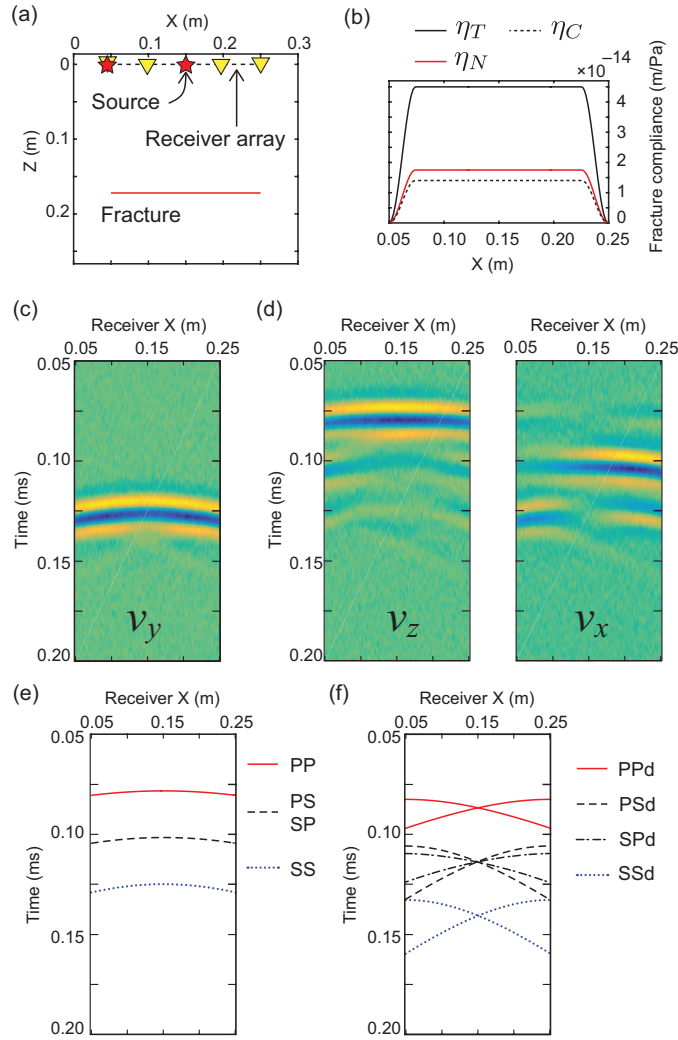


Figure 1: (a) Configuration of numerical modeling. (b) Fracture compliances along the fracture. Tangential (η_T), normal (η_N) and coupling (η_C) compliances are shown. (c) Modeled shot gather showing SH wavefield. (d) Modeled shot gather for P-SV wavefield. (e) Calculated traveltimes of specular reflections. (f) Calculated traveltimes of non-specular reflections from the edges of the fracture. PPd: diffracted P wave due to incident P wave, PSd: diffracted S wave due to incident P wave, SPd: diffracted P wave due to incident S wave, and SSd: diffracted S wave due to incident S wave.

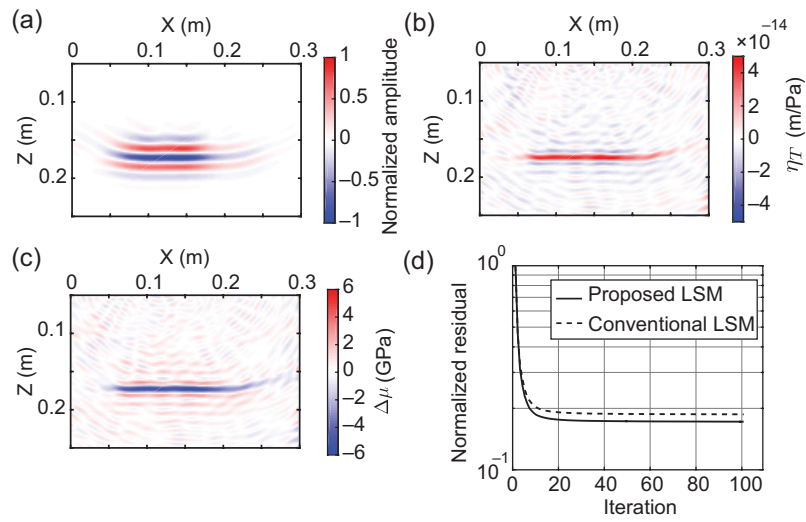


Figure 2: Imaging results for SH wavefield; (a) Initial gradient without inversion, (b) proposed LSM involving linear-slip theory, and (c) conventional LSM without linear-slip theory. (d) Residuals at each CG iteration using the proposed LSM and the conventional LSM.

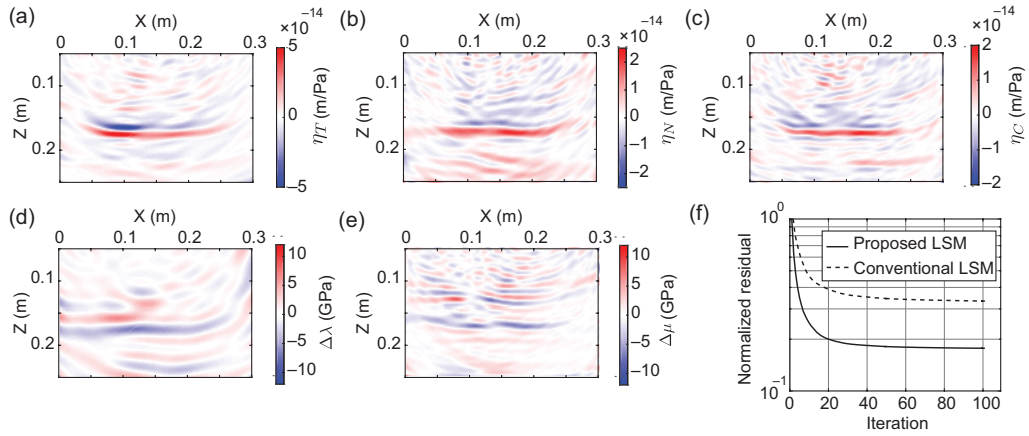


Figure 3: Imaging results for P-SV wavefield using the proposed LSM; (a) tangential compliance, (b) normal compliance, and (c) coupling compliance. (d)–(e) Imaging results using the conventional LSM for the perturbation in λ and μ . (f) Residuals at each CG iteration using the proposed LSM and the conventional LSM.

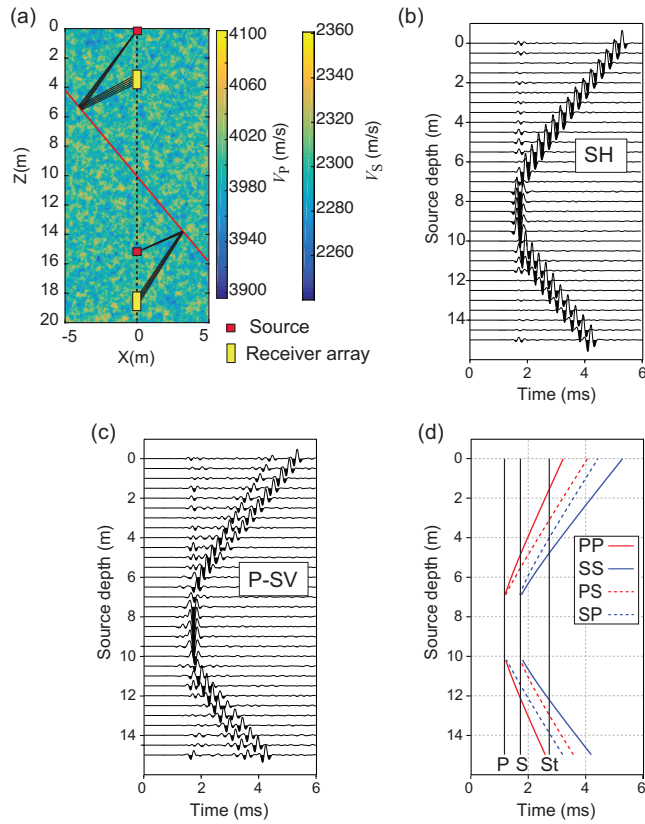


Figure 4: (a) Configuration of borehole acoustic measurements. First and last source-receiver geometries and the background velocity model are shown. The red line indicates the fracture. The dotted line indicates the location of the borehole. (b) Numerically modeled dipole data (SH wavefield) at the first receiver due to varying source depths. (c) Same as (b) but for P-SV wavefield. (d) Calculated traveltimes of direct waves (P and S), Stoneley wave (St), and reflected waves from the fracture (PP, SS, PS and SP).

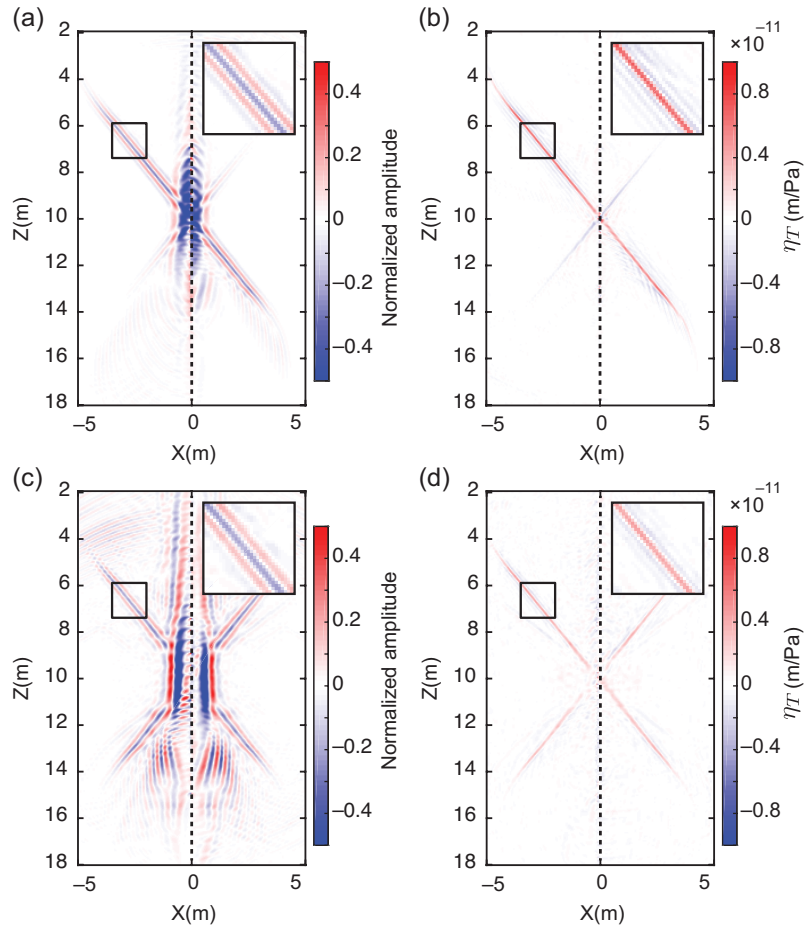


Figure 5: Imaging results using SH wavefield in dipole acoustic logging data; (a) Initial gradient without inversion, (b) the proposed LSM. (c),(d) Same as (a),(b) but using P-SV wavefield.

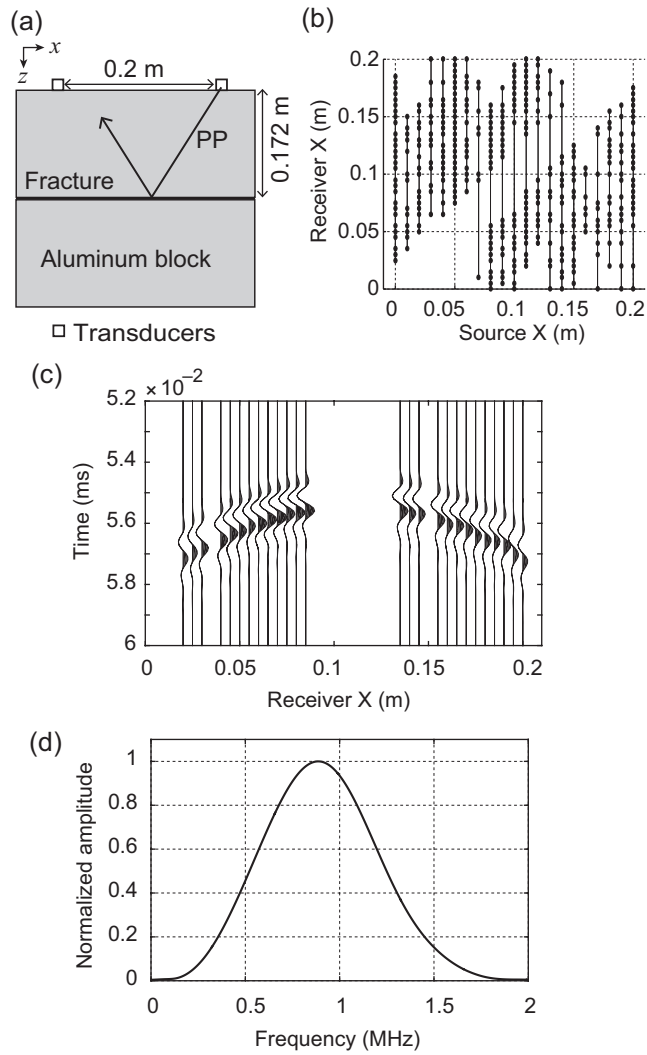


Figure 6: (a) Configuration of laboratory experiments. The fracture aperture is created using $100 \mu\text{m}$ thick spacers. (b) Source–receiver geometry for the measured data. (c) An example of the measured PP reflection data for a source located at 0.11 m. (d) Frequency spectrum of (c).

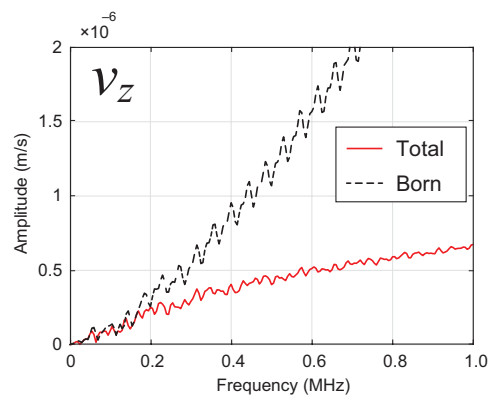


Figure 7: Frequency spectrum of the numerically modeled reflection response, representing the laboratory geometry and the fracture compliances. The total response and the Born approximation are shown.

—

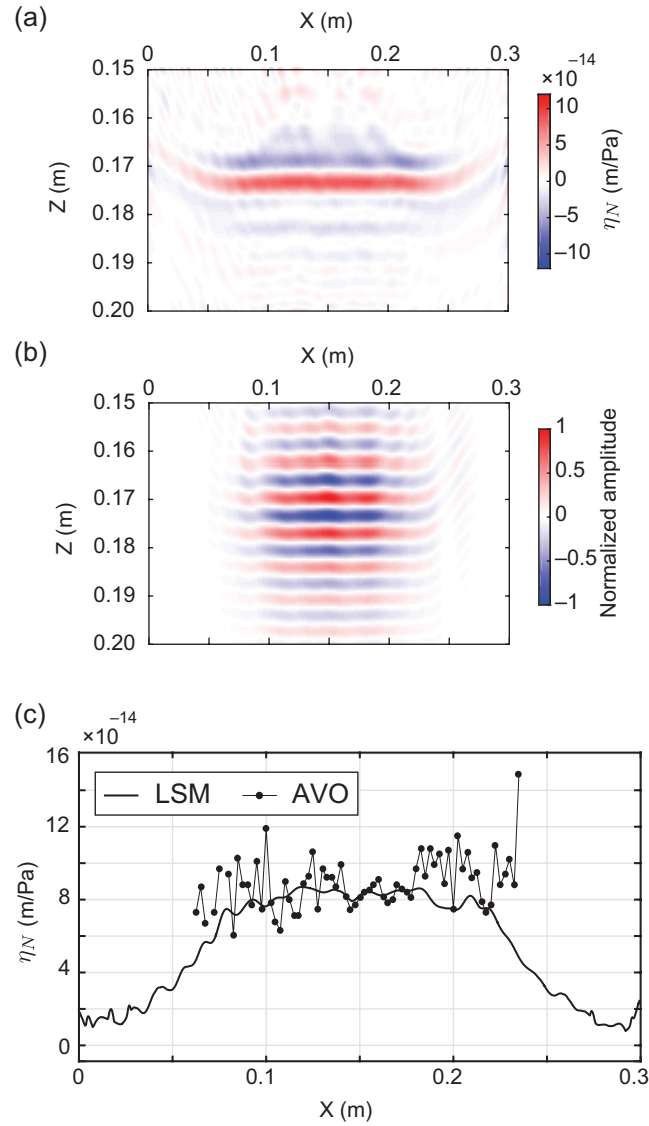


Figure 8: (a) Imaging results on laboratory experimental data of a homogeneously wet fracture using the proposed LSM (50–500 KHz). (b) Imaging result using initial gradient. (c) Estimated normal fracture compliance along the fracture from the proposed LSM and the AVO inversion from Minato et al. (2018).

–

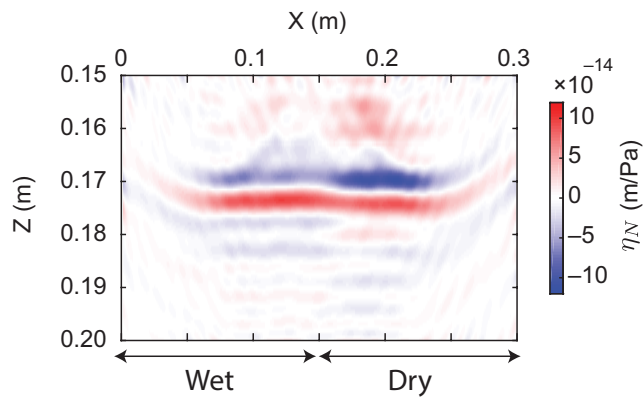


Figure 9: Imaging results on laboratory experimental data of a heterogeneously wet fracture using the proposed LSM (50–500 KHz).

–

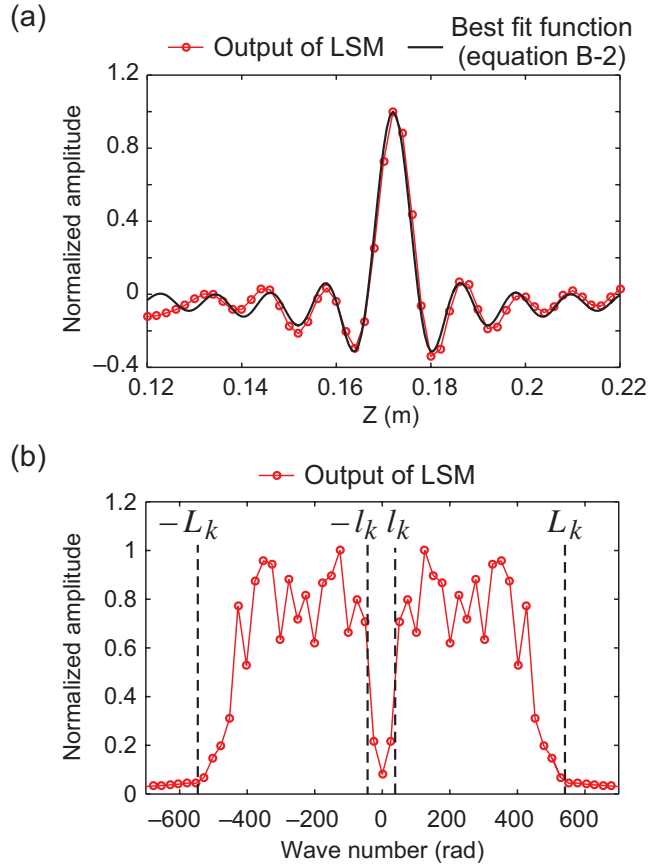


Figure B-1: (a) An example of the estimation of L_k and l_k in equation B-2. The red line shows the output of LSM at $x = 0.15$ m followed by normalization of the amplitude, and the black line shows the best-fit curve using equation B-2 with $(L_k, l_k) = (543.50, 40.84)$. (b) The Fourier spectrum of (a) and the detected values of L_k and l_k .

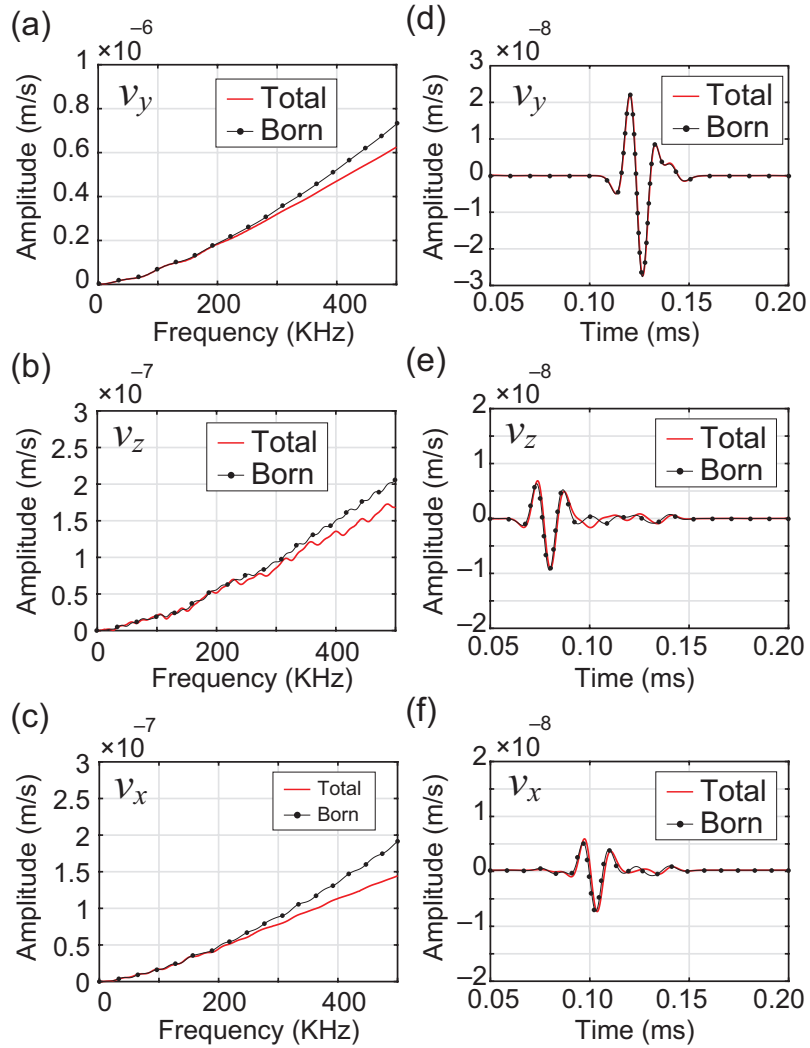


Figure C-1: Born approximated response (Born) and true response (Total) for zero-offset record in the configuration of Figure 1a. (a),(b),(c) Modeled Green's functions for SH wavefield (v_y) and P-SV wavefield (v_z and v_x). (d),(e),(f) Time-domain responses of (a),(b),(c) after convolution of Ricker wavelet with 50 KHz center frequency.

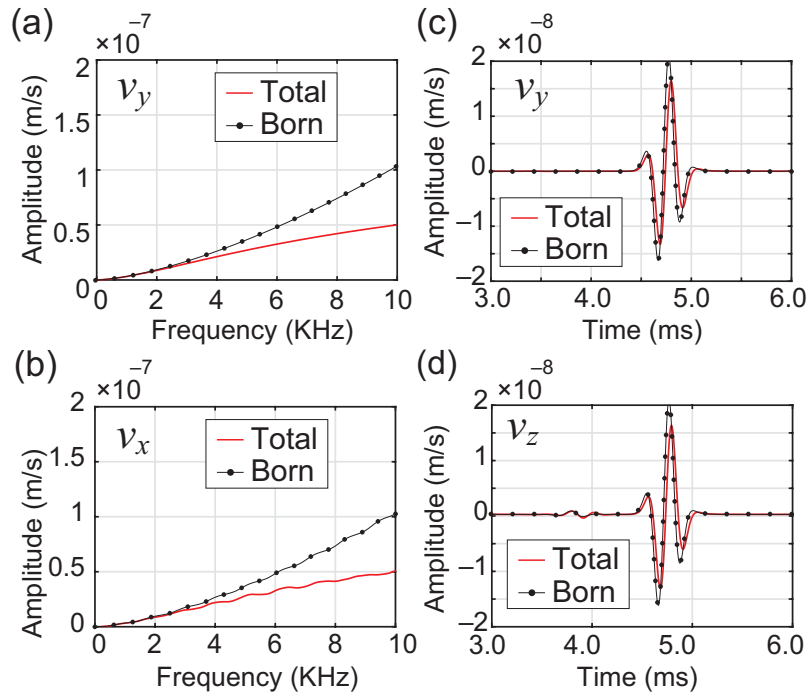


Figure C-2: Born approximated response (Born) and true response (Total) for zero-offset record in the configuration of Figure 4a. (a),(b) Modeled Green's functions for SH wavefield (v_y) and P-SV wavefield (v_x). (c),(d) Time-domain responses of (a),(b) after convolution of Ricker wavelet with 3 KHz center frequency.

—